NeuroImage: Clinical 48 (2025) 103866

Contents lists available at ScienceDirect

NeuroImage: Clinical

journal homepage: www.elsevier.com/locate/ynicl

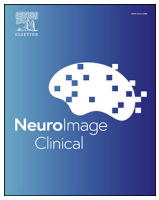

Mapping iron content and white matter integrity in the anterior thalamic radiations across Huntington's disease stages

Montserrat Domingo-Ayllón [a,b], Clara Garcia-Gorro [a], Nadia Rodriguez-Dechicha [d], Irene Vaquer [d], Matilde Calopa [e], Ruth de Diego-Balaguer [a,c,f], Estela Camara [a,b,*]

[a] Cognition and Brain Plasticity Unit [Bellvitge Biomedical Research Institute – IDIBELL], 08097 L'Hospitalet de Llobregat, Barcelona, Spain
[b] Radiology Department, University Hospital Joan XXIII, Tarragona, Spain
[c] Institut de Neurociències. Department of Cognition, Development and Education Psychology, Universitat de Barcelona, Barcelona, Spain
[d] Hestia Duran i Reynals. Hospital Duran i Reynals, Hospitalet de Llobregat (Barcelona), Spain
[e] Movement Disorders Unit, Neurology Service, Hospital Universitari de Bellvitge, Barcelona, Spain
[f] ICREA (Catalan Institute for Research and Advanced Studies), Barcelona, Spain

ARTICLE INFO

Keywords:
Anterior thalamic radiation
Huntington's disease
Neurodegeneration
Relaxometry
Diffusion tensor
Machine learning models
Biomarkers

ABSTRACT

Huntington's disease (HD) is characterized by progressive neurodegeneration, often accompanied by disrupted iron regulation and altered white matter (WM) integrity. This study investigates iron content and microstructural changes in the anterior thalamic radiations (ATR) across different HD stages. Thirty-one gene carriers and twenty-four controls underwent neuropsychological assessment and 3 T-MRI scanning, including relaxometry and diffusion tensor imaging (DTI) sequences to assess iron content and WM microstructure. ATR changes were examined using average and along-the-tract analyses, with ANOVA and post-hoc Tukey tests to identify group differences and Spearman correlations to evaluate clinical associations. Machine-learning models were applied to assess the potential of MRI metrics as diagnostic biomarkers for HD, focusing on disease stage differentiation and presymptomatic detection. Premanifest individuals exhibited increased iron content and enhanced WM integrity bilaterally, while manifest patients maintained elevated left ATR iron levels alongside bilateral WM degeneration. Both ATRs contribute to the clinical manifestations of HD, including cognitive impairment and neuropsychiatric disturbances. Both along-the-tract relaxometry and DTI metrics emerged as promising biomarkers for distinguishing HD subgroups and identifying presymptomatic individuals. These findings highlight the interplay between iron dysregulation and WM disruption in HD, offering potential pathways for early diagnosis and targeted therapeutic strategies.

1. Introduction

The anterior thalamic radiations (ATRs) are critical structural pathways within the cortico-basal ganglio-thalamo-cortical loops (Cho et al., 2015; Kakou et al., 2017; Wakana et al., 2003), connecting the anterior and mediodorsal thalamic nuclei to frontal lobes, and their physiological role is primarily linked to cognition and emotion control (Fama and Sullivan, 2015; Jankowski et al., 2013; Mitchell, 2015; Pergola et al., 2018).

In Huntington's disease (HD), the primary neuropathological insult of the medium spiny neurons of the striatum (Han et al., 2010; Vonsattel et al., 1985) is accompanied by a complex interplay of factors, including a reduction of brain-derived neurotrophic factor (BDNF) (Han et al., 2010; Muller and Leavitt, 2014) and an excess of glutamate signalled from the cortex towards the basal ganglia (Bano et al., 2011). Together, these mechanisms are thought to contribute to basal ganglia degeneration, disrupting the cortico-basal ganglio-thalamo-cortical loops (Blumenstock and Dudanova, 2020; Novak et al., 2015) and leading to secondary degeneration of the ATRs that may be due to anterograde transynaptic degeneration (Montoya-Filardi et al., 2022). Dysfunction

Abbreviations: AD, axial diffusivity; AOO, age of onset; ATR, anterior thalamic radiation; CAP, CAG-Age Product; DTI, diffusion tensor imaging; FA, fractional anisotropy; FDR, false discovery rate; MD, mean diffusivity; mHtt, mutant huntingtin; RD, radial diffusivity; R2*, relaxometry based on T2-GRE sequences; UHDRS, Unified Huntington's Disease Rating Scale; WM, white matter.

* Correspondence author at: Cognition and Brain Plasticity Unit, IDIBELL (Institut d'Investigació Biomèdica de Bellvitge), Feixa Larga S/N, 08907 L'Hospitalet de Llobregat, (Barcelona), Spain.
E-mail address: ecamara@idibell.cat (E. Camara).

https://doi.org/10.1016/j.nicl.2025.103866
Received 7 April 2025; Received in revised form 5 August 2025; Accepted 12 August 2025
Available online 14 August 2025

or disruption of the ATRs has been implicated in the cognitive and psychiatric symptoms (Martinez-Horta et al., 2016; McColgan and Tabrizi, 2018; Papoutsi et al., 2014) observed in gene carriers at various stages of the disease, even before the onset of motor symptoms.

Macroscopically, HD is characterized by grey matter (GM) and white matter (WM) atrophy, as stated by neuropathology (Reiner et al., 2011; Waldvogel et al., 2014) and evidenced by voxel-based morphometric (VBM) MRI studies (Aylward et al., 2011; Faria et al., 2016; Furlong et al., 2020; Stoffers et al., 2010). Early in the disease, degeneration predominantly affects the dorsal striatum, along with its associated white matter tracts (Aylward et al., 2011; Domínguez D et al., 2013; Tabrizi et al., 2013). As the disease progresses, this degeneration extends beyond the striatum, involving the cerebral cortex and other deep brain structures (Aylward et al., 2004; McColgan et al., 2015; Niccolini, 2014; Novak et al., 2015). The microstructural pathology of WM in HD is complex, including oligodendrocyte dysfunction with developmental myelination impairments and myelin breakdown (Bardile et al., 2019; Blockx et al., 2012b, 2012a; Gomez-Tortosa et al., 2001) as well as early axonal degeneration (Li et al., 2001). Compensatory increases in oligodendrocyte density have also been observed during early disease stages, reflecting the multifaceted nature of WM pathology in HD (Bardile et al., 2019; Blockx et al., 2012b, 2012a; Gomez-Tortosa et al., 2001).

Diffusion tensor imaging (DTI) studies have detected microstructural WM tract anomalies in presymptomatic and symptomatic stages, before atrophy could be evident (Bourbon-Teles et al., 2019; Casella et al., 2022, 2020; Della Nave et al., 2010; Estevez-Fraga et al., 2021; Matsui et al., 2015; Odish et al., 2015; Phillips et al., 2014; Rosas et al., 2018), highlighting the importance of investigating early-stage neurodegenerative process. Manifest HD patients consistently exhibit significant microstructural disruptions in both ATRs (Bourbon-Teles et al., 2019; Estevez-Fraga et al., 2021; Gregory et al., 2019; Odish et al., 2015; Phillips et al., 2014; Rosas et al., 2018; Saba et al., 2017), but inconsistent findings have been found in presymptomatic stages regarding the specific nature of these alterations. For example, Phillips et al. identified increases in RD and AD in both ATRs (Phillips et al., 2014), while Rosas et al. observed elevated RD exclusively in the right ATR near disease onset (Rosas et al., 2018). These findings suggest that ATR degeneration may occur early in HD, but the mechanisms underlying WM degeneration remain incompletely understood.

Iron is a key player in different neurodegenerative diseases, including HD, but its precise role remains elusive. Iron can act as both a primary and secondary trigger in the neurodegenerative process (Muller and Leavitt, 2014; Ward et al., 2014). On one hand, iron is involved in oxidative stress, neuroinflammation and ferroptosis (Latunde-Dada, 2017; Wu et al., 2018). Alternatively, iron accumulation as a result of the neurodegenerative process itself may aggravate the main neuropathological traits (Kempuraj et al., 2016; Simmons et al., 2007; Thomsen et al., 2015). In the context of HD, mutant huntingtin (mHtt) has been related to disruptions in iron metabolism, including increased iron uptake (Niu et al., 2018) and iron accumulation in microglia inducing the proinflammatory microglial phenotype (Kempuraj et al., 2016; Simmons et al., 2007; Thomsen et al., 2015). Despite these findings, the specific role of iron in HD neurodegeneration, and the relationship between iron dysregulation and WM degeneration is not fully understood.

Disruptions in both WM integrity and iron homeostasis are recognized as critical contributors to the neurodegenerative process underlying HD (Li and Conforti, 2013; Muller and Leavitt, 2014; Sun et al., 2022). However, their interrelations and interactions are not fully understood. It is possible that WM degeneration induces iron accumulation, which may, in turn, drive an ongoing loop where both factors interact and exacerbate one another (Kempuraj et al., 2016; Stephenson et al., 2018; Thomsen et al., 2015). Alternatively, primary iron accumulation could act as a trigger for WM degeneration, initiating the cascade of interrelated pathological processes (Latunde-Dada, 2017; Mi et al., 2019; Muhoberac and Vidal, 2013; Wu et al., 2018). These mechanisms might also function independently, without directly influencing one another, or they could become interdependent at specific stages of the disease. Clarifying the potential relationships between WM degeneration and iron alterations may advance our understanding of HD pathology and contribute to the identification of new therapeutic targets.

This study focuses on ATR degeneration in HD, employing a cross-sectional assessment of diffusion and relaxometry in controls and gene carriers. The assessment of presymptomatic and symptomatic stages aims to clarify the relationship between iron accumulation and WM disturbance, being either metachronous or synchronous and either interrelated or independent, in order to uncover the dynamics of the neurodegenerative mechanisms underlying HD, opening new avenues for future research directions. The spatial assessment comparing right vs left ATR investigates the presence of potential differential hemispheric vulnerability. Both average and along-the-tract methodologies were used to explore their sensitivities in detection of differences. Finally, translating MRI findings into clinical applications is critical. Machine learning algorithms were used to integrate WM and iron-level features from ATR, with the goal of identifying biomarkers for earlier diagnosis during presymptomatic stages and as endpoints in future clinical trials.

2. Materials and methods

2.1. Participants

This study is part of a larger research project conducted between 2013 and 2016, during which clinical and MRI data were collected at two time points. Specifically, the present study focuses on the second time point, as T2*-weighted relaxometry images were only acquired at this stage. Due to participant attrition between the two time points, some individuals from the initial cohort were not available for follow-up. The first time point was composed by 35 controls, 22 presymptomatic gene carriers, and 25 symptomatic HD patients. The final sample used in this study consisted of 55 participants, comprising 31 gene carriers (8 males, 23 females) and 24 healthy controls (13 males, 11 females) matched for gender ($\chi^2_{(1,n=55)} = 3.49$, $p = 0.062$), age ($t_{(49.62)} = -0.08$, $p = 0.940$) and years of education ($t_{(50.13)} = 0.36$, $p = 0.722$). Gene carriers were further grouped into premanifest ($N = 13$) and manifest ($N = 18$) stages based on their Unified Huntington's Disease Rating Scale (UHDRS) diagnostic confidence score for motor abnormalities. When comparing the different subgroups, significant differences in age and gender distribution were observed (age $F_{(2,52)} = 3.67$, $p = 0.032$; gender $\chi^2_{(2,n=55)} = 7.72$, $p = 0.021$). Specifically, gender distribution differed significantly between controls and premanifest participants, with a higher proportion of females in the premanifest subgroup ($\chi^2_{(1,n=37)} = 5.89$, $p = 0.015$). Age also differed significantly between premanifest and manifest participants, with the premanifest subgroup being younger ($t_{(26.77)} = -2.87$, $p = 0.008$), as expected due to the natural course of disease progression in HD. No significant differences were found in age or gender between controls and manifest patients, nor in age between controls and premanifest participants (see Table 1 for participants' demographic details).

None of the participants reported previous history of neurological disorders other than HD in patients. All participants were right-handed and provided written informed consent to participate in this study, in accordance with the Helsinki Declaration of 1975.

2.2. Clinical evaluation

Gene carriers underwent a set of clinical assessments carried out by clinicians specialized in movement disorders (Table 1). The UHDRS total motor score was used to assess the severity of motor symptoms. The verbal fluency test (FAS), the Symbol Digit Modalities Test (SDMT), the Trail Making Test (TMT), and the Stroop word-reading, color-naming and interference test were administered as part of the cognitive section

Table 1
Sociodemographic and clinical characteristics of study participants.

	Controls	Premanifest	Manifest	Gene-carriers	Controls vs Gene carriers	ANOVA / Chi-square	Controls vs Premanifest	Controls vs Manifest	Premanifest vs Manifest
N	24	13	18	31					
Sex (M/F)	13/11	1/12	7/11	8/23	X^2(1,N = 55) = 3.49 (p = 0.062)	**X^2(2,N = 55) = 7.72 (p = 0.021)**	**X^2(1,N = 37) = 5.89 (p = 0.015)**	X^2(1,N = 42) = 0.45 (p = 0.504)	X^2(1,N = 31) = 2.38 (p = 0.123)
Age (years)	46.42 ± 11.14	40.62 ± 9.73	51 ± 10.23	46.65 ± 11.15	t(49.62) = -0.08 (p = 0.940)	**F(2,52) = 3.67 (p = 0.032)**	t(27.79) = 1.64 (p = 0.111)	t(38.30) = -1.38 (p = 0.175)	**t(26.77) = -2.87 (p = 0.008)**
Education (years)	12.54 ± 2.89	13.54 ± 2.67	11.33 ± 2.87	12.26 ± 2.95	t(50.13) = 0.36 (p = 0.722)	F(2,52) = 2.35 (p = 0.105)	t(26.53) = -1.05 (p = 0.301)	t(36.91) = 1.35 (p = 0.186)	t(27.10) = 2.20 (p = 0.036)
CAG		42.77 ± 2.17	44.17 ± 3.13	43.58 ± 2.81					t(28.97) = -1.47 (p = 0.153)
CAP		81.30 ± 16.97	112.13 ± 18.86	99.20 ± 23.58					**t(27.50) = -4.76 (p = 0.000)**
Age of onset		50.17 ± 8.15	45.98 ± 9.59	47.74 ± 9.12					t(28.14) = 1.31 (p = 0.201)
UHDRS-motor		0.38 ± 0.87 (N = 13)	22.94 ± 13.78 (N = 17)	13.17 ± 15.31 (N = 30)					**t(16.17) = -6.73 (p = 0.000)**
UHDRS-cognitive		328 ± 46.25 (N = 13)	192 ± 62.22 (N = 15)	255.14 ± 87.91 (N = 28)					**t(25.47) = 6.62 (p = 0.000)**
UHDRS-functional		24.92 ± 0.28 (N = 13)	19.18 ± 5.43 (N = 17)	21.67 ± 4.97 (N = 30)					**t(16.11) = 4.35 (p = 0.000)**
Cognitive reserve		15.54 ± 3.78 (N = 13)	11.56 ± 3.71 (N = 18)	13.23 ± 4.18 (N = 31)					**t(25.74) = 2.92 (p = 0.007)**
Stroop Interferences		49.08 ± 8.57 (N = 13)	28.80 ± 11.93 (N = 15)	38.21 ± 14.58 (N = 28)					**t(25.21) = 5.21 (p = 0.000)**
TMT(B-A) direct		36.23 ± 36.53 (N = 13)	105.88 ± 63.50 (N = 17)	75.70 ± 63.32 (N = 30)					**t(26.28) = -3.78 (p = 0.001)**
PBA-Enroll									
- Depression Component		1.58 ± 3.00 (N = 12)	2.76 ± 3.35 (N = 17)	2.28 ± 3.21 (N = 29)					Z = 79, p = 0.274
- Irritability Component		0.67 ± 1.78 (N = 12)	2.06 ± 4.39 (N = 17)	1.48 ± 3.57 (N = 29)					Z = 78, p = 0.204
- Psychosis Component		0.17 ± 0.58 (N = 12)	0.31 ± 1.01 (N = 17)	0.25 ± 0.84 (N = 29)					Z = 92, p = 0.762
- Apathy Component		1.42 ± 2.71 (N = 12)	3.00 ± 3.32 (N = 17)	2.34 ± 3.13 (N = 29)					Z = 60.5, p = 0.058
- Dysexecutive Component		1.42 ± 2.02 (N = 12)	2.94 ± 2.73 (N = 17)	2.31 ± 2.54 (N = 29)					Z = 65, p = 0.088

Data presented as *mean* ± *standard deviation*. Premanifest and manifest division based on Unified Huntington's Disease Rating Scale diagnostic confidence score for motor abnormalities.
CAG = length of cytosine-adenine-guanine base repeats of the mutated allele; CAP = standardized CAG-age product; F = females; M = males; N = number of participants; PBA=Problem Behaviours Assessment; UHDRS-cognitive = Unified Huntington's Disease Rating Scale total cognitive score; UHDRS-motor = Unified Huntington's Disease Rating Scale total motor score. Age of onset calculated according to Langbehn formula.

of the UHDRS. CAG-Age Product (CAP) score, computed as CAP = 100*age*(CAG–35.5)/627 (Ross et al., 2014), was used as a proxy of disease burden secondary to accumulated exposure to mHtt. PBA-s (Problem Behaviour Assessment – Short) test (Craufurd D et al., 2001; Enroll-HD, n.d.) from Enroll-HD composed by 5 composite scores (depression, irritability/aggression, psychosis, apathy, and dysexecutive) was administered to assess for psychiatric symptoms.

2.3. MRI acquisition and processing

MRI data was acquired at 3 T whole-body MRI scanner (Siemens Magnetom Trio), using a 32-channel phased array head coil. The sequences performed included: a conventional high-resolution 3D T1 MPRAGE sequence [208 sagittal slices, TR 1970 ms, TE 2.34 ms, IT 1050 ms, flip angle 9°, FOV 25.6 cm, 1 mm isotropic voxel with no gap between slices]; a dual spin-echo diffusion imaging sequence with GRAPPA (reduction factor of 4) cardiac gating [60 axial slices, TR 680 ms, TE 92 ms, 2 mm isotropic voxels, no gap, FOV 23.6 cm, 64 non-collinear directions using a b-value of 1500 s/mm^2 interleaved with 9 non-diffusion b = 0 images]; and six consecutive T2*-weighted gradient echo-planar images [60 axial slices, TR 5000 ms, bandwidth 1120 Hz/Pz, FOV 25.6 cm, matrix size 128*128*60, flip angle 90°, 2 mm isotropic voxels] at different TE (6, 12, 20, 30, 45 and 60 ms).

2.4. Data analysis

2.4.1. T2*-weighted images processing

T2*-weighted volumes were post-processed accordingly to

previously published methods (Baudrexel et al., 2009). In order to obtain the voxel-based relaxometry maps, each of the six T2*-weighted volumes were linearly aligned with the mean T2*-weighted volume; a voxel-by-voxel nonlinear least-squares fitting of the six TEs was performed to obtain a mono-exponential signal decay curve and relaxometry volumes were based on relaxation rates (i.e. relaxation rates R2*=1/T2*x1000). Finally, iron images (R2*) were registered into native DTI (Diffusion Tensor Imaging) space.

2.4.2. Pre-processing of DTI data

Diffusion-weighted images were automatically processed using FreeSurfer v6.0 software (http://surfer.nmr.mgh.harvard.edu/). More specifically, head motion and eddy-current correction were firstly performed, and the gradient matrix was rotated accordingly (Leemans and Jones, 2009). Subsequently, affine intra-subject alignment was performed between diffusion-weighted and anatomical images, and to an MNI152 template (Greve and Fischl, 2009).

The diffusion tensor was then reconstructed using a standard least squares tensor estimation algorithm and its corresponding eigenvalues were extracted to calculate the fractional anisotropy (FA), mean, radial and axial diffusivities (MD, RD, AD) maps.

2.4.3. Tractography dissections: Anterior thalamic radiation

Virtual in vivo DTI reconstruction of ATR was carried out using TRActs Constrained by UnderLying Anatomy (TRACULA), available as part of FreeSurfer image processing (Yendiki et al., 2011) and previously validated in HD (Rosas et al., 2018). TRACULA is a new gold-standard method for the automated reconstruction of the main WM pathways based on a global probabilistic approach using anatomical priors derived from a training set of manually labeled tracts in healthy individuals. These priors are based on the relative positioning of each tract with respect to surrounding anatomical structures, defined by FreeSurfer's automated parcellation of each individual. Specifically, the anatomical model is aligned with the dissection protocol proposed by Wakana et al., 2003, which defines the ATR pathway using a coronal slice selected at the level of the genu of the corpus callosum, where one ROI is placed on the anterior limb of the internal capsule, and a second ROI is defined at the anterior edge of the pons to include the entire thalamus. Streamlines extending outside the expected pathway, such as those crossing into the contralateral hemisphere via the corpus callosum, are excluded. While manual tractography approaches rely on explicit ROI placement, TRACULA automates this process, embedding prior anatomical knowledge into its reconstruction algorithms.

This approach enabled the reconstruction of the ATR's volumetric distribution in native space, allowing for the extraction of both average and along-the-tract values of diffusion and relaxometry parameters. This processing pipeline included cortical and subcortical parcellation, correction of diffusion images for eddy current distortions, and ATR reconstruction for each participant. Quality control of the reconstructed ATRs was performed by a certified neuroradiologist (MDA) through visual inspection of each participant's T1-weighted anatomical and diffusion data, along with the corresponding parcellations and final ATR reconstructions.

2.4.4. Statistical analysis

The statistical analysis was performed with R software (R Core Team, 2024). Demographic differences were assessed using independent sample *t* tests for numerical variables, Wilcoxon tests for ordinal variables (PBA-Enroll scores) and chi-square or Fisher's exact test for gender (nominal variable).

Although HD is clinically diagnosed based on the onset of motor symptoms, neurodegeneration, accompanied by cognitive and neuropsychiatric symptoms, often begins well before motor onset (Martinez-Horta et al., 2016). Therefore, in our cross-sectional assessment of iron accumulation and WM integrity, we performed group comparisons across disease stages (controls, premanifest, and manifest HD). However, for analyses exploring clinical correlations, we treated HD gene carriers (both premanifest and manifest) as part of a continuous disease spectrum, rather than categorically distinct subgroups.

To investigate cross-sectional differences in ATR microstructure and relaxometry across disease stages, both mean and along-the-tract measures of DTI indexes and relaxometry of each ATR were assessed using a permutational analysis of variance (ANOVA). Group comparisons were conducted among three subgroups: healthy controls, presymptomatic gene carriers, and symptomatic (manifest) patients.

For the mean analysis, the permutational ANOVAs included subgroup as the independent variable of interest, age (factorized into three categories: $\leq$40, 41–50, >50 years) and gender as covariates. For the along-the-tract analysis, diffusion metrics and relaxometry were sampled at 45 points for the right ATR and at 47 points for the left ATR. This approach follows the standard protocol implemented in TRACULA, a tractography-based pipeline within FreeSurfer software (http://surfer.nmr.mgh.harvard.edu/), which automatically reconstructs major white matter pathways and samples diffusion measures along their length. Including the different points conforming the ATRs for each individual in the along-the-tract models warranted two phenomena. First, it incorporates spatial information along the tract given that WM tracts are not anatomically or microstructurally homogenous; diffusion and relaxometry can vary systematically depending on the anatomical position within the tract. Second, it increases statistical power by providing a higher number of observations per participant. This increased within-subject data density was accounted for by modelling subject as a random effect by the Error (1/subject) in the permutational ANOVAs framework. In these along-the-tract ANOVAs, subgroup was the independent variable of interest. Covariates included age (factorized into three categories: $\leq$40, 41–50, >50 years), gender and point, that is, the index position along the ATR (45 levels for the right ATR, 47 for the left). The point variable was included to control for potential confounding effects of anatomical position within the ATR, as MRI values may vary along the tract independent of pathology.

Pairwise permutation post-hoc tests were performed to assess the pairwise subgroup differences in DTI indexes and relaxometry for each ATR. The test statistic used in these comparisons was the maximum test statistic (maxT) and p-values were adjusted using false discovery rate (FDR) correction.

To address potential hemispheric susceptibility, right-left differences in both mean and along-the-tract measures of DTI indexes and relaxometry were assessed using permutational ANOVA. The independent variable of interest was the interaction between subgroup and hemisphere (right/left). Factorized age and gender were included as covariates, and, for the along-the-tract analysis, point (tract location) was also added as a covariate. Subject-level random effects were accounted for using the 'Error (1/subject)' term. Pairwise permutation post-hoc tests were applied to the subgroup x hemisphere interaction to explore the pattern of lateralization within each subgroup. Also, right-left and left–right differences in along-the-tract values were computed for each subgroup and compared using pairwise permutation post-hoc tests. Again, the maxT statistic was used, and FDR correction was applied to all p-values.

To understand the interrelationship between DTI metrics and relaxometry, partial Spearman correlations were performed between along-the-tract measures of WM indexes and relaxometry values, controlling by gender and factorized age in controls and by gender and CAP score in gene carriers, to disentangle their interdependence eliminating the possible influence of the illness in this interdependence. Moreover, paired partial Spearman correlations were also conducted to assess the interdependence of each paired combination of DTI parameters and relaxometry values, controlling for all the other variables.

In order to investigate the relationship between ATR microstructure and neurological deficits in gene carriers, partial Spearman correlations were conducted between average MRI-derived parameters (analysed separately for each ATR) and a range of clinical measures. CAP score and

UHDRS-functional score were used as markers of overall disease progression. Motor symptoms were evaluated using the UHDRS-motor score. Cognitive function was assessed using UHDRS-cognitive score, as well as performance on the TMT (B–A) and Stroop Interference tests. Psychiatric disturbances were examined through PBA subdomains scores. The correlations concerning disease progression were adjusted for gender. All other correlations were performed twice, once controlling for gender to assess associations potentially modulated by disease progression, and another controlling for both gender and disease burden (CAP score) to investigate associations that may reflect the specific physiological role of the ATR.

The FDR was used to correct pairwise permutation post-hoc tests and partial Spearman correlations. Results statistically significant with a p-adjusted (p-adj) value of < 0.05 were those reported in the manuscript, unless specified otherwise.

Finally, to evaluate the potential role of MRI metrics as biomarkers, three machine-learning models, namely boosted logistic regression (BLR), quadratic discriminant analysis (QDA) and support vector machines with radial basis function kernel (SVMR), were assessed in three scenarios. The first scenario included the three subgroups to assess their capability to differentiate among subgroups. The second included the control and the presymptomatic subgroups, and the third, the presymptomatic and the symptomatic subgroups, with the aim to focus on the clinically relevant questions: the ability of the biomarkers in detecting presymptomatic subjects (positive class) regarding controls in order to initiate preventive measures and regarding symptomatic patients in order to diagnose precociously the beginning of the illness. The dataset consisted of 2475 observations (45 points * 55 individuals) for each MRI metric (10 metrics in total, 5 metrics for each ATR). These observations were divided in two subsets: 80 % for training the model (training dataset) and the remaining 20 % for testing (test dataset) to assess the generalization of the trained models in unseen data. Each model in each scenario was trained twice using cross-validation, once with and once without recursive feature elimination (RFE). The models' effectiveness was evaluated using confusion matrices with their derived statistical parameters (accuracy, kappa, precision, F1-score, recall or sensitivity, and specificity) and ROC-AUC curves to provide insight into classification accuracy and predictive power.

3. Results

3.1. Microstructural and iron characterization of ATR

3.1.1. Global differences in white matter ATR microstructure and iron levels

Diffusion-derived average metrics revealed significant bilateral group differences in MD (Right: $F(2,45) = 11.62$, p-adj < 0.001; Left: $F(2,45) = 9.08$, p-adj $= 0.002$), RD (Right: $F(2,45) = 8.88$, p-adj $= 0.001$; Left: $F(2,45) = 7.82$, p-adj $= 0.003$), and AD (Right: $F(2,45) = 8.64$, p-adj $= 0.001$; Left: $F(2,45) = 6.70$, p-adj $= 0.005$). Post-hoc analysis showed that these differences were primarily driven by overall higher diffusivity values in manifest HD. Specifically, manifest HD patients exhibited significant increases in MD (Right: maxT $= 3.31$, p-adj $= 0.003$; Left: maxT $= 3.13$, p-adj $= 0.005$), RD (Right: maxT $= 2.96$, p-adj $= 0.006$; Left: maxT $= 2.74$, p-adj $= 0.009$), and AD (Right: maxT $= 3.00$, p-adj $= 0.008$; Left: maxT $= 2.93$, p-adj $= 0.010$) when compared to controls. Similarly, significant differences were also observed when comparing manifest HD patients to premanifest individuals, with increased MD (Right: maxT $= 2.93$, p-adj $= 0.005$; Left: maxT $= 2.87$, p-adj $= 0.006$), RD (Right: maxT $= 2.86$, p-adj $= 0.006$; Left: maxT $= 2.97$, p-adj $= 0.009$), and AD (Right: maxT $= 2,45$, p-adj $= 0.022$; Left: maxT $= 1.91$, n.s.) for manifest patients.

No significant average differences among subgroups were present for FA (Right: $F(2,45) = 1.24$, p-adj $= 0.299$; Left: $F(2,45) = 2.48$, p-adj $= 0.119$) or R2* (Right: $F(2,45) = 2.26$, p-adj $= 0.146$; Left: $F(2,45) = 0.45$, p-adj $= 0.642$) (see Supplementary materials Table 1).

3.1.2. Differences along white matter ATR microstructure and iron levels

Group along-the-tract effects were in accordance to those obtained in the average assessment showing significant bilateral group differences in mean (Right: $F(2,2116) = 277.09$, p-adj < 0.001; Left: $F(2,2170) = 156.29$, p-adj < 0.001), radial (Right: $F(2,2116) = 179.07$, p-adj < 0.001; Left: $F(2,2170) = 121.33$, p-adj < 0.001), and axial (Right: $F(2,2116) = 204.49$, p-adj < 0.001; Left: $F(2,2170) = 98.28$, p-adj < 0.001) diffusivities. In addition, unlike the global analysis, group differences were also detected bilaterally in FA (Right: $F(2,2116) = 21.65$, p-adj < 0.001; Left: $F(2,2170) = 33.03$, p-adj < 0.001) and R2* values (Right: $F(2,2116) = 29.42$, p-adj < 0.001; Left: $F(2,2170) = 23.48$, p-adj < 0.001).

Further post-hoc analysis showed that manifest patients exhibited significant bilateral along-the-tract increases in MD, RD and AD compared to both premanifest individuals (MD: Right maxT $= 9.39$, p-adj < 0.001, Left maxT $= 7.56$, p-adj < 0.001; RD: Right maxT $= 8.48$, p-adj < 0.001, Left maxT $= 7.58$, p-adj < 0.001; AD: Right maxT $= 8.08$, p-adj < 0.001 Left maxT $= 5.07$, p-adj < 0.001) and controls (MD: Right maxT $= 10.22$, p-adj < 0.001, Left maxT $= 8.47$, p-adj < 0.001; RD: Right maxT $= 8.26$, p-adj < 0.001, Left maxT $= 6.80$, p-adj < 0.001; AD: Right maxT $= 10.35$, p-adj < 0.001, Left maxT $= 8.93$, p-adj < 0.001) in accordance with findings from the average assessment. In addition, manifest patients showed a significant along-the-tract decrease in FA in both ATR when compared to premanifest patients (Right maxT $= -3.99$, p-adj < 0.001; Left maxT $= -5.14$, p-adj < 0.001).

Interestingly, premanifest individuals exhibited a bilateral increase in FA values compared to controls (Right maxT $= 3.04$, p-adj $= 0.004$; Left maxT $= 4.98$, p-adj < 0.001), that was accompanied by a significant bilateral decrease in RD (Right maxT $= -2.45$, p-adj $= 0.014$; Left maxT $= -2.68$, p-adj $= 0.007$), and a left increase in AD (Left maxT $= 2.87$, p-adj $= 0.004$), differences not detected in the average analysis. Given that presymptomatic participants were, on average, younger than controls (mean age: controls $= 46$ vs. presymptomatic $= 40$ years; $p = 0.111$), a post-hoc pairwise permutation test was conducted to further examine whether the FA differences persisted when controlling for age. Specifically, age was factorized into three categories (≤ 40, 41–50, and > 50 years), and group comparisons were conducted within each category. In the right ATR, significant FA increases in presymptomatic participants were observed in those aged ≤ 40 years (maxT $= 2.87$, p-adj $= 0.004$) and > 50 years (maxT $= 2.40$, p-adj $= 0.045$), but not in the 41–50 group (maxT $= 0.01$, p-adj $= 0.991$). In the left ATR, significant FA increases were detected in presymptomatic individuals older than 40, both in the 41–50 age group (maxT $= 3.84$, p-adj < 0.001) and the > 50 group (maxT $= 4.38$, p-adj < 0.001), while no differences were found in participants aged ≤ 40 (maxT $= 0.57$, p-adj $= 0.572$). Additionally, because the presymptomatic subgroup included a higher proportion of women (1/13 men) compared to controls (13/24 men), another post-hoc pairwise permutation test was conducted separately for males and females to account for potential gender bias. In both ATRs, increased FA in presymptomatic individuals was observed exclusively in women (right ATR: males maxT $= 0.65$, p-adj $= 0.550$; females maxT $= 2.34$, p-adj $= 0.029$; left ATR: males maxT $= 0.92$, p-adj $= 0.481$; females maxT $= 5.10$, p-adj < 0.001).

In contrast to the findings from the average analysis, manifest patients demonstrated a significant decrease in R2* for both ATR compared to premanifest individuals (Right: maxT $= -5.53$, p-adj < 0.001; Left: maxT $= -2.42$, p-adj $= 0.015$) and for the right ATR compared to controls (Right: maxT $= -2.25$, p-adj $= 0.025$). However, manifest patients exhibited a significant increase in R2* for the left ATR compared to controls (Left: maxT $= 3.86$, p-adj < 0.001). Additionally, premanifest individuals also exhibited a significant increment of R2* bilaterally compared to controls (Right: maxT $= 4.52$, p-adj < 0.001; Left: maxT $= 6.98$, p-adj < 0.001).

Results are summarized in Supplementary materials Table 2. Fig. 1 depicts the along-the-tract values of both ATR separately.

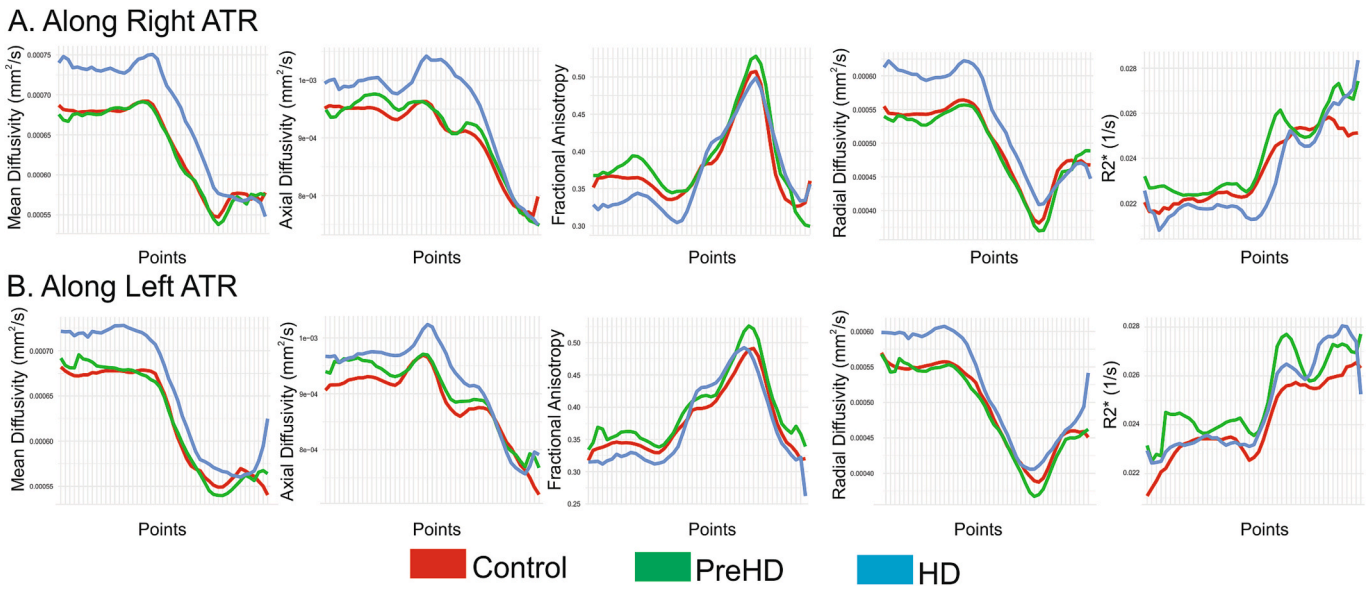

Fig. 1. Along-the-tract profiles of MRI metrics in the anterior thalamic radiations. Separate line plots are shown for each MRI metric, representing the mean along the tract values across subgroups, **(A)** for the right ATR and **(B)** for the left ATR. ATR: anterior thalamic radiation. HD: symptomatic patients. PreHD: pre-symptomatic individuals.

3.1.3. Interhemispheric differences in white matter ATR microstructure and iron levels

Regarding right-left asymmetries assessed in each group separately, no differences were observed in any of the average MRI measurements across the three subgroups (see Supplementary materials Table 3). However, right-left along-the-tract asymmetries were detected for R2*, MD and AD (see Supplementary materials Table 4). Specifically, the left ATR showed increased along-the-tract R2* for the three subgroups. The right ATR exhibited an increased along-the-tract MD for the three subgroups, and an increased along-the-tract AD for controls and manifest patients. The loss of AD asymmetry in premanifest individuals may be related with the increased AD observed in the left ATR.

Given these differences of composition between ATRs, for illustrative purposes, the right-left differences were used for the assessment of diffusivities, and the left–right differences for the analysis of R2* (see Fig. 2). HD patients showed greater right-left differences for AD, MD and RD compared to both premanifest individuals (AD difference: maxT = 5.21, p-adj < 0.001; MD difference: maxT = 4.25, p-adj < 0.001; RD difference: maxT = 2.29, p-adj = 0.033) and controls (AD difference: maxT = 4.43, p-adj < 0.001; MD difference: maxT = 4.87, p-adj < 0.001; RD difference: maxT = 3.27, p-adj = 0.003). Moreover, HD patients and premanifest individuals had greater left–right R2* differences compared to controls (maxT = 7.16, p-adj < 0.001 for HD patients, maxT = 3.59, p-adj < 0.001 for premanifest individuals). HD patients also presented greater left–right R2* differences compared to premanifest subjects (maxT = 2.87, p-adj = 0.004). No right-left differences were detected for FA.

3.1.4. Coupling between white matter ATR microstructure and iron levels

To investigate the interdependence between R2*-relaxometry and DTI metrics, partial Spearman correlation analyses were conducted across all three subgroups (controls, presymptomatic, and symptomatic gene carriers), considering all the data points that form the length of both ATR. Analyses were controlled for gender and factorized age in controls, and for gender and CAP score in gene carriers, to reduce potential confounding effects of gender and disease burden in this

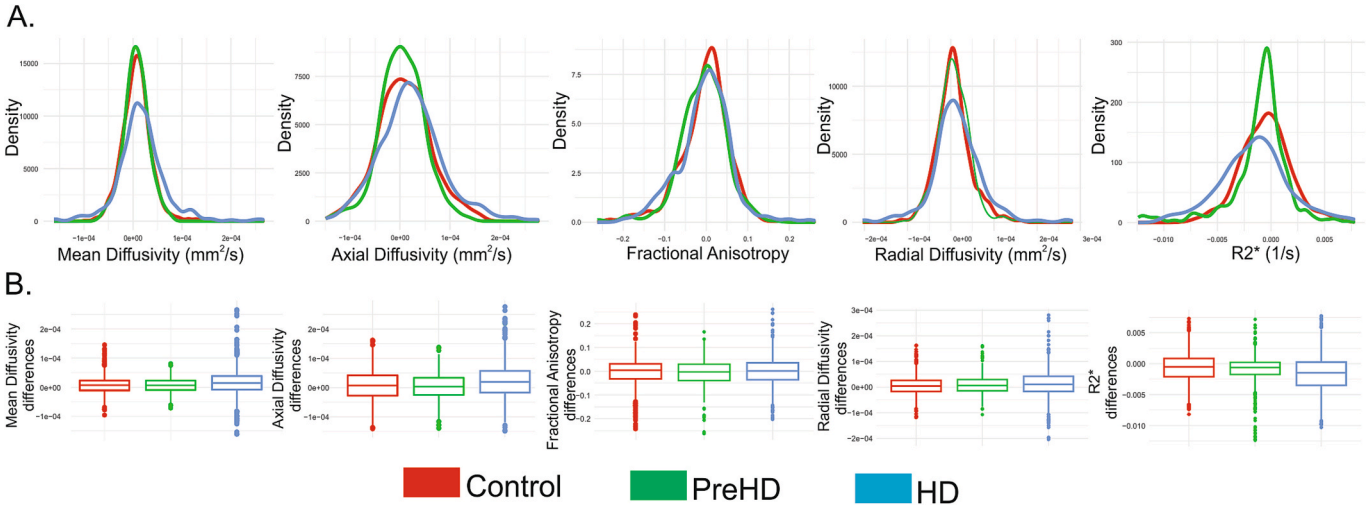

Fig. 2. Right-Left differences in along-the-tract of MRI metrics. Separate density plots **(A)** and boxplots **(B)** for each MRI metric illustrate right-minus-left differences in along-the-tract mean values across subgroup. HD: symptomatic patients. PreHD: presymptomatic subjects.

interdependence.

Across all subgroups and hemispheres, R2* consistently showed weak to strong negative correlations with diffusivity metrics. In both the right and left ATR, R2* was significantly inversely associated with AD, RD and MD. Specifically, in controls, R2* correlated negatively with AD (Right r = − 0.377, p-adj < 0.001, Left r = − 0.468, p-adj < 0.001), RD (Right r = − 0.499, p-adj < 0.001, Left r = − 0.464, p-adj < 0.001) and MD (Right r = − 0.549, p-adj < 0.001, Left r = − 0.521, p-adj < 0.001). Similar patterns were observed in presymptomatic gene carriers (AD: Right r = − 0.576, p-adj < 0.001, Left r = − 0.436, p-adj < 0.001; RD: Right r = − 0.543, p-adj < 0.001, Left r = − 0.494, p-adj < 0.001; MD: Right r = − 0.634, p-adj < 0.001, Left r = − 0.530, p-adj < 0.001) and symptomatic HD patients (AD: Right r = − 0.473, p-adj < 0.001, Left r = − 0.542, p-adj < 0.001; RD: Right r = − 0.495, p-adj < 0.001, Left r = − 0.361, p-adj < 0.001; MD: Right r = − 0.576, p-adj < 0.001, Left r = − 0.467, p-adj < 0.001). In contrast, R2* showed very weak to weak positive correlations with FA in all groups (Controls: Right r = 0.200, p-adj < 0.001, Left r = 0.222, p-adj < 0.001; PreHD: Right r = 0.176, p-adj < 0.001, Left r = 0.325, p-adj < 0.001; HD: Right r = 0.149, p-adj < 0.001, Left r = 0.111, p-adj = 0.006). Fig. 3 depicts the correlations between R2* and each of the DTI metrics for both ATR separately.

Furthermore, paired partial correlations were conducted to examine the unique association between each DTI metric and R2*, while controlling for the influence of the remaining DTI metrics and covariates (i.e., gender and factorized age in controls, gender and CAP score in gene carriers).

In the right ATR, for controls, R2* demonstrated a small-to-moderate negative correlation with FA (r = –0.192, p-adj < 0.001), a small positive correlation with AD (r = 0.108, p-adj = 0.002), and very weak negative associations with both RD (r = –0.071, p-adj = 0.046) and MD (r = –0.071, p-adj = 0.046). In presymptomatic gene carriers, R2* showed a moderate negative association with FA (r = –0.213, p-adj < 0.001) and a small-to-moderate negative correlation with RD (r = –0.158, p-adj < 0.001), while correlations with AD (r = –0.042, p-adj = 0.456) and MD (r = 0.010, p-adj = 0.819) were non-significant. In symptomatic individuals, similar associations were observed, with R2* negatively correlated with FA (r = –0.214, p-adj < 0.001) and RD (r = –0.095, p-adj = 0.025); correlations with AD (r = 0.028, p-adj = 0.529) and MD (r = –0.026, p-adj = 0.529) remained non-significant.

In the left ATR, for controls, R2* was weakly to moderately negatively correlated with FA (r = –0.129, p-adj < 0.001) and RD (r = –0.100, p-adj = 0.011), and showed a trend-level negative association with AD (r = –0.072, p-unc = 0.026, p-adj = 0.077), while no significant correlation was found with MD (r = 0.046, p-adj = 0.301). In presymptomatic gene carriers, no significant correlations were found between R2* and any DTI metric (AD: r = –0.006, p-adj = 0.890; RD: r = –0.043, p-adj = 0.460; MD: r = –0.034, p-adj = 0.480; FA: r = –0.042, p-adj = 0.460). In symptomatic patients, R2* showed a trend-level negative association with MD (r = –0.088, p-unc = 0.018, p-adj = 0.070), with no significant associations with AD (r = –0.070, p-adj = 0.142), RD (r = 0.043, p-adj = 0.415), or FA (r = –0.032, p-adj = 0.470).

3.2. Clinical correlates

3.2.1. Relationship between white matter ATR microstructure and iron levels with neuropsychological assessments in gene carriers

Reported correlations include those statistically significant with an adjusted p-value (p-adj) < 0.05, as well as those showing a statistical trend, defined as an uncorrected p-value (p-unc) < 0.05 but a non-significant adjusted p-value (p-adj < 0.10). This broader approach aims to provide a more comprehensive overview, acknowledging that some potentially clinically relevant associations might be overlooked with stricter statistical thresholds (see Supplementary materials Table 5, and Fig. 4 for details).

Regarding disease progression, significant positive correlations were observed between CAP score and both MD and RD of the right (MD: r = 0.538, p-adj = 0.023; RD: r = 0.548, p-adj = 0.020) and left ATRs (MD: r = 0.517, p-adj = 0.036; RD: r = 0.515, p-adj = 0.037). A trend toward a positive association was also found between CAP score and AD of the right ATR (r = 0.488, p-unc = 0.016, p-adj = 0.064). In contrast, UHDRS

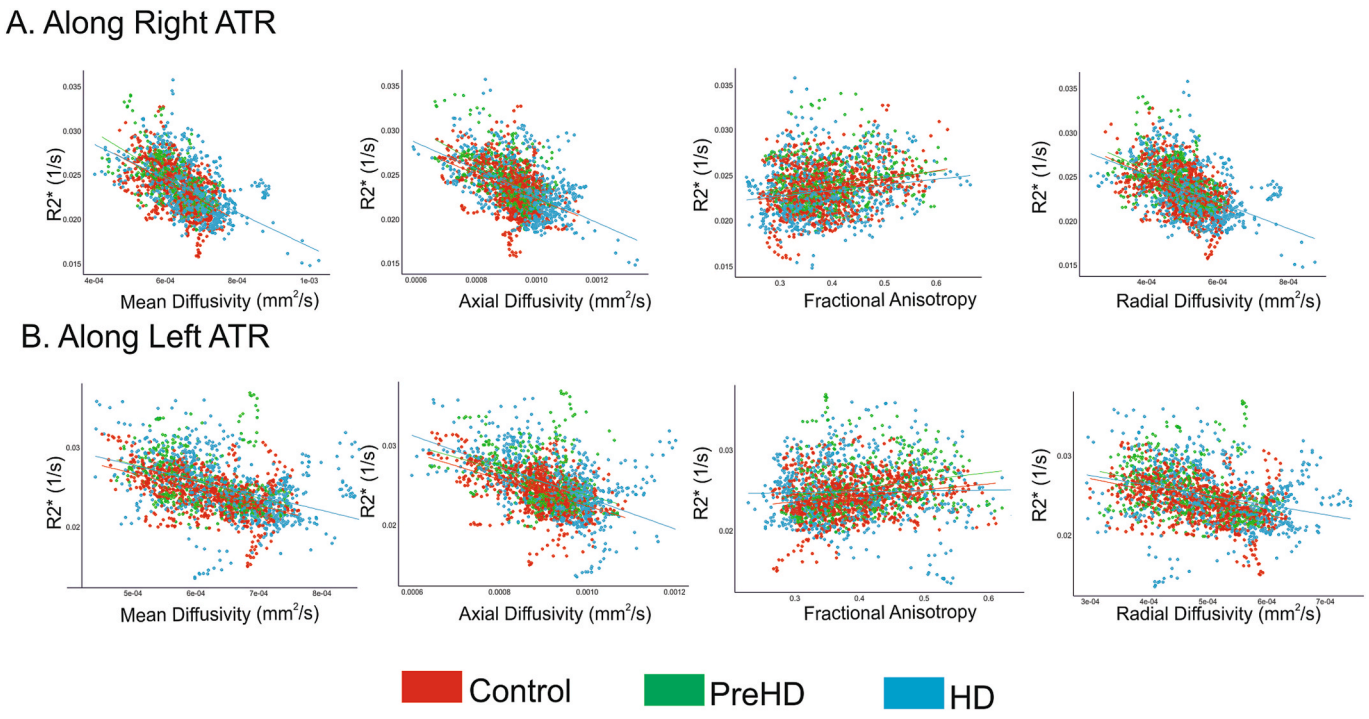

Fig. 3. Correlations plots of the along-the-tract values between R2* relaxametry and each DTI metric, **(A)** for the right ATR and **(B)** for the left ATR. For illustrative purposes, these plots are not adjusted for specific covariates. ATR: anterior thalamic radiation. HD: symptomatic patients. PreHD: presymptomatic individuals.

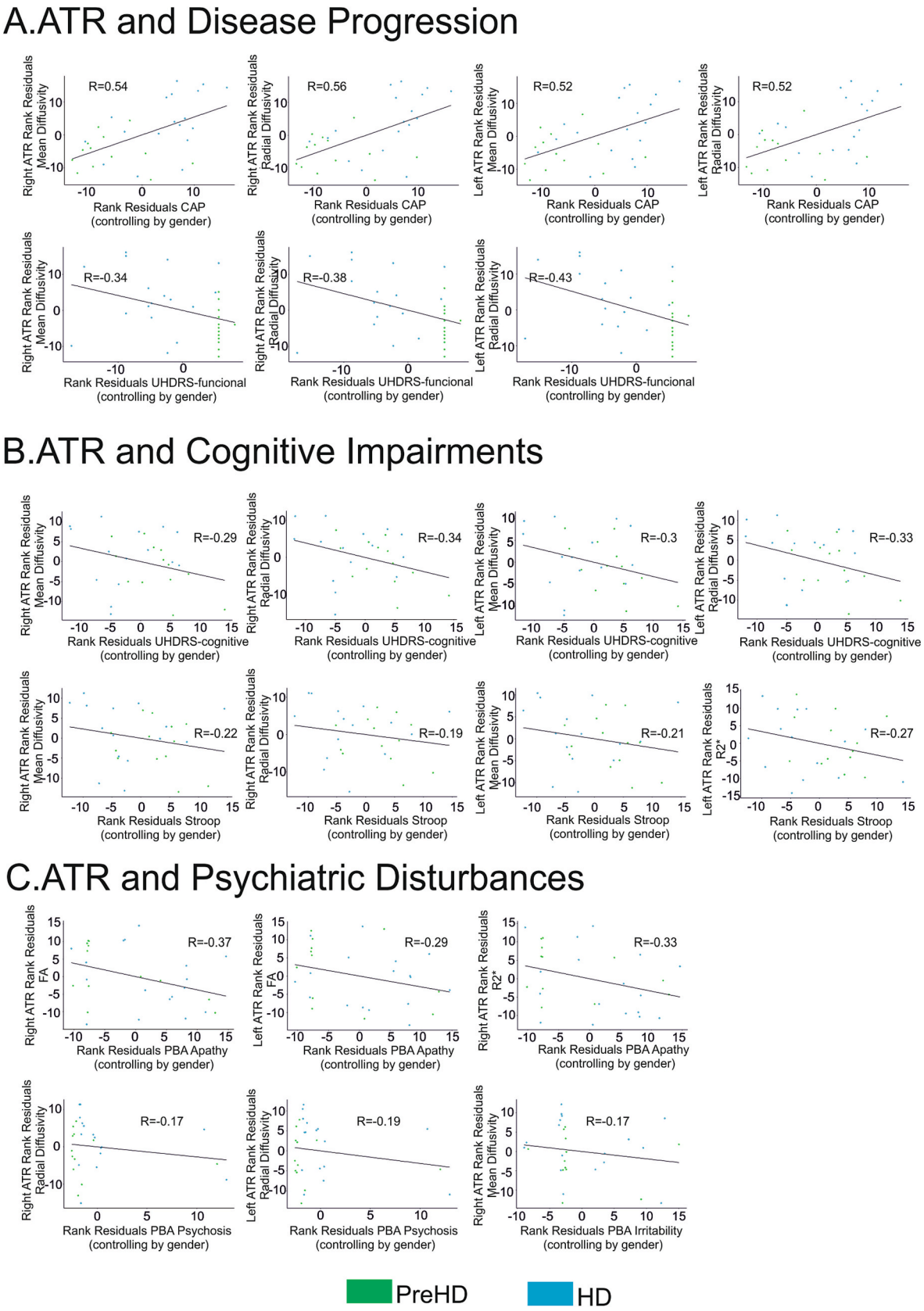

Fig. 4. Partial Spearman correlation plots between average MRI metrics and clinical measures. Scatter plots illustrate Pearson correlations between residual ranks of average MRI metrics (adjusted for controlling factors) and clinical scores assessing disease progression **(A)**, cognitive impairments **(B)** and psychiatric disturbances **(C)**. ATR: anterior thalamic radiation. HD: symptomatic patients. PreHD: presymptomatic individuals.

functional scores showed significant negative correlations with MD of the right ATR (r = -0.344, p-adj = 0.023) and with RD of both ATRs (Right: r = -0.383, p-adj = 0.015; Left: r = -0.426, p-adj = 0.007). A trend toward a negative correlation was also observed between UHDRS functional scores and MD of the left ATR (r = -0.293, p-unc = 0.019, p-adj = 0.054).

In relation to motor symptoms, UHDRS-motor scores showed a trend toward positive correlation with RD in both the right (r = 0.429, p-unc = 0.049, p-adj = 0.095) and left (r = 0.441, p-unc = 0.041, p-adj = 0.082) ATRs.

Cognitive assessments showed significant associations with ATR microstructure. In the right ATR, MD and RD were significantly negatively correlated with UHDRS cognitive scores (MD: r = -0.480, p-adj < 0.001; RD: r = -0.521, p-adj < 0.001), as well as Stroop interference performance (MD: r = -0.404, p-adj = 0.013; RD: r = -0.390, p-adj = 0.015). In the left ATR, similar patterns were observed for MD and RD showing significant negative correlations with UHDRS cognitive (MD: r = -0.513, p-adj < 0.001; RD: r = -0.515, p-adj < 0.001) and Stroop interference scores (MD: r = -0.417, p-adj = 0.013; RD: r = -0.363, p-adj = 0.025). Additionally, MD and RD of the left ATR showed a trend toward positive association with TMT (B-A) scores (MD: r = 0.479, p-unc = 0.022, p-adj = 0.055; RD: r = 0.466, p-unc = 0.028, p-adj = 0.062). Moreover, AD of the right ATR showed negative trends with UHDRS cognitive scores (r = -0.310, p-unc = 0.016, p-adj = 0.064) and Stroop interference (r = -0.352, p-unc = 0.007, p-adj = 0.064).

When controlling for disease burden (CAP score) to explore the ATR's physiological role in cognitive function, several associations remained significant. In the right ATR, MD and RD demonstrated significant negative correlations with UHDRS cognitive scores (MD: r = -0.288, p-adj = 0.010; RD: r = -0.336, p-adj < 0.001) and Stroop interference performance (MD: r = -0.217, p-adj = 0.023; RD: r = -0.190, p-adj = 0.040). In the left ATR, both MD and RD were negatively correlated with UHDRS cognitive scores (MD: r = -0.301, p-adj = 0.010; RD: r = -0.328, p-adj < 0.001), and MD also negatively correlated with Stroop interference (r = -0.206, p-adj = 0.036). Moreover, R2*-relaxometry of the left ATR showed a significant negative correlation with Stroop performance (r = -0.275, p-adj = 0.020). Trend-level negative correlations were observed between Stroop interference performance and RD of the left ATR (r = -0.154, p-unc = 0.024, p-adj = 0.062), and with AD of the right ATR (r = -0.199, p-unc = 0.010, p-adj = 0.064).

Concerning psychiatric disturbances, apathy scores showed a significant negative correlation with FA of the right ATR (r = -0.367, p-adj = 0.050). When controlling for disease burden, PBA-apathy scores were significantly negatively correlated with FA of both the right (r = -0.369, p-adj < 0.001) and left ATRs (r = -0.327, p-adj < 0.001), and with R2*-relaxometry of the right ATR (r = -0.295, p-adj = 0.020). A trend-level negative association was also observed between apathy and AD of the right ATR (r = -0.182, p-unc = 0.014, p-adj = 0.064). PBA-psychosis scores were significantly negatively correlated with RD of both the right (r = -0.171, p-adj = 0.049) and left ATRs (r = -0.193, p-adj = 0.037), and showed trend-level negative associations with MD of both the right (r = -0.141, p-unc = 0.030, p-adj = 0.067) and left ATRs (r = -0.133, p-unc = 0.035, p-adj = 0.070). PBA-irritability scores showed a significant negative correlation with MD of the right ATR (r = -0.175, p-adj = 0.049), and trend-level negative associations with MD of the left ATR (r = -0.175, p-unc = 0.017, p-adj = 0.054) and with RD of the right ATR (r = -0.144, p-unc = 0.030, p-adj = 0.067). Lastly, trend-level negative correlations were found between PBA-depression scores and both MD (r = -0.152, p-unc = 0.026, p-adj = 0.065) and RD (r = -0.159, p-unc = 0.023, p-adj = 0.057) of the right ATR, and MD (r = -0.140, p-unc = 0.033, p-adj = 0.070) and RD (r = -0.153, p-unc = 0.026, p-adj = 0.062) of the left ATR.

3.2.2. *Machine learning models in the assessment of MRI metrics as biomarkers*

In the first scenario with the inclusion of the three subgroups (controls, presymptomatic, and symptomatic patients), models without RFE obtained better performance than those with RFE. Notably, BLR and SVMR models did not eliminate any feature during RFE, given that all variables had a relative weight, necessary to correctly separate subgroups (see Supplementary materials Fig. 1A). The most discriminant variables were AD and MD of both ATR, as well as RD and R2* of the right ATR. Among the models, SVMR without RFE achieved the highest performance, with an accuracy of 70.3 %, a Cohen's Kappa coefficient of 0.53, and AUC values of 87.3 % for the macro-average and of 87.9 % for the micro-average. The sensitivities and specificities for each subgroup were the following: 80.9 % and 68.1 % for controls, 38.5 % and 92.9 % for presymptomatic subjects, and 78.9 % and 90.5 % for symptomatic patients. Precision and F1-scores were as follows: 66.4 % and 72.9 % for controls, 62.7 % and 47.7 % for presymptomatic subjects, and 80.2 % and 79.6 % for symptomatic patients. Overall statistics and subgroup-specific statistics for the models evaluated in this scenario are summarised in tables 2 and 3, respectively. The ROC-AUC curve with the corresponding confusion matrix for SVMR model without RFE is shown in Fig. 5A.

In the second scenario, which focused on differentiating presymptomatic individuals from controls, models with RFE performed better than those without RFE. Interestingly, the most discriminating variables for distinguishing these subgroups, based on RFE analysis, were the following in order of importance: left R2*, right R2*, left FA, right FA, and left AD (see Supplementary materials Fig. 1B). The SVMR with RFE provided the highest accuracy and performance values. The selected variables included R2*, FA, and AD from both ATRs, and RD from the left ATR, with R2* and FA of both ATRs and AD of the left ATR being the most discriminative. The model achieved an accuracy of 75.2 % with a Cohen's Kappa coefficient of 0.44, and an AUC value of 81.3 %. Sensitivity and specificity were 58.3 % and 84.3 %, respectively, while precision and F1-score were 66.7 % and 62.2 %, respectively.

In the third scenario, which differentiated presymptomatic subjects from symptomatic patients, models with RFE again performed better than those without RFE. Key variables for distinguishing these subgroups were the following in order of importance: right MD, right AD, right RD, left MD, right R2*, left AD and left RD (see Supplementary materials Fig. 1C). The SVMR with RFE was the model with the highest accuracy and better performance measures. All variables were selected by RFE, with the most discriminant being MD, AD, RD and R2* of the right ATR, and MD of the left ATR. This model achieved an accuracy of 88.2 % with a Cohen's Kappa coefficient of 0.76, and an AUC of 95.8 %. Sensitivity and specificity were 90.6 % and 86.5 % respectively, while precision and F1-score were 82.9 % and 86.6 % respectively. Table 4 summarises the statistics for the models of the second and third

Table 2
Overall statistics of the machine learning models obtained from test datasets of the along-the-tract MRI metrics of both ATR including the three subgroups.

	Accuracy	Kappa	AUC (macro-average)	AUC (micro-average)
LBR without RFE	0.646	0.449	0.741	0.756
LBR with RFE	0.624	0.359	0.690	0.725
QDA without RFE	0.585	0.330	0.735	0.757
QDA with RFE	0.545	0.225	0.679	0.716
SVMR without RFE	0.703	0.526	0.873	0.879
SVMR with RFE	0.698	0.517	0.869	0.875

AUC: area under the curve; LBR: logistic boost regression, QDA: quadratic discriminant analysis; RFE: recursive feature elimination; SVMR: support vector machines with radial basis function kernel.

Table 3
Statistics by subgroups of the machine learning models obtained from tests datasets of the along-the-tract MRI metrics of both ATR including the three subgroups.

	Balanced Accuracy	Sensitivity	Specificity	Precision	Recall	F1-score	AUC
LBR without RFE							
Class..Control	0.717	0.686	0.749	0.676	0.686	0.681	0.736
Class..PreHD	0.674	0.508	0.841	0.452	0.508	0.478	0.694
Class..HD	0.771	0.675	0.866	0.740	0.675	0.706	0.793
LBR with RFE							
Class..Control	0.685	0.661	0.753	0.661	0.661	0.661	0.719
Class..PreHD	0.511	0.471	0.822	0.393	0.471	0.429	0.669
Class..HD	0.768	0.667	0.856	0.742	0.667	0.702	0.809
QDA without RFE							
Class..Control	0.653	0.770	0.537	0.564	0.770	0.651	0.680
Class..PreHD	0.632	0.344	0.920	0.569	0.344	0.429	0.729
Class..HD	0.686	0.511	0.861	0.642	0.511	0.569	0.797
QDA with RFE							
Class..Control	0.590	0.888	0.293	0.494	0.888	0.635	0.615
Class..PreHD	0.500	0.000	1.000	NA	0.000	NA	0.647
Class..HD	0.699	0.481	0.916	0.736	0.481	0.582	0.774
SVMR without RFE							
Class..Control	0.745	0.831	0.664	0.658	0.831	0.734	0.823
Class..PreHD	0.657	0.333	0.945	0.653	0.333	0.441	0.868
Class..HD	0.847	0.789	0.898	0.789	0.789	0.789	0.908
SVMR with RFE							
Class..Control	0.741	0.815	0.668	0.656	0.815	0.727	0.869
Class..PreHD	0.645	0.354	0.936	0.630	0.354	0.453	0.875
Class..HD	0.845	0.789	0.901	0.795	0.789	0.792	0.869

AUC: area under the curve; LBR: logistic boost regression, QDA: quadratic discriminant analysis; RFE: recursive feature elimination; SVMR: support vector machines with radial basis function kernel.

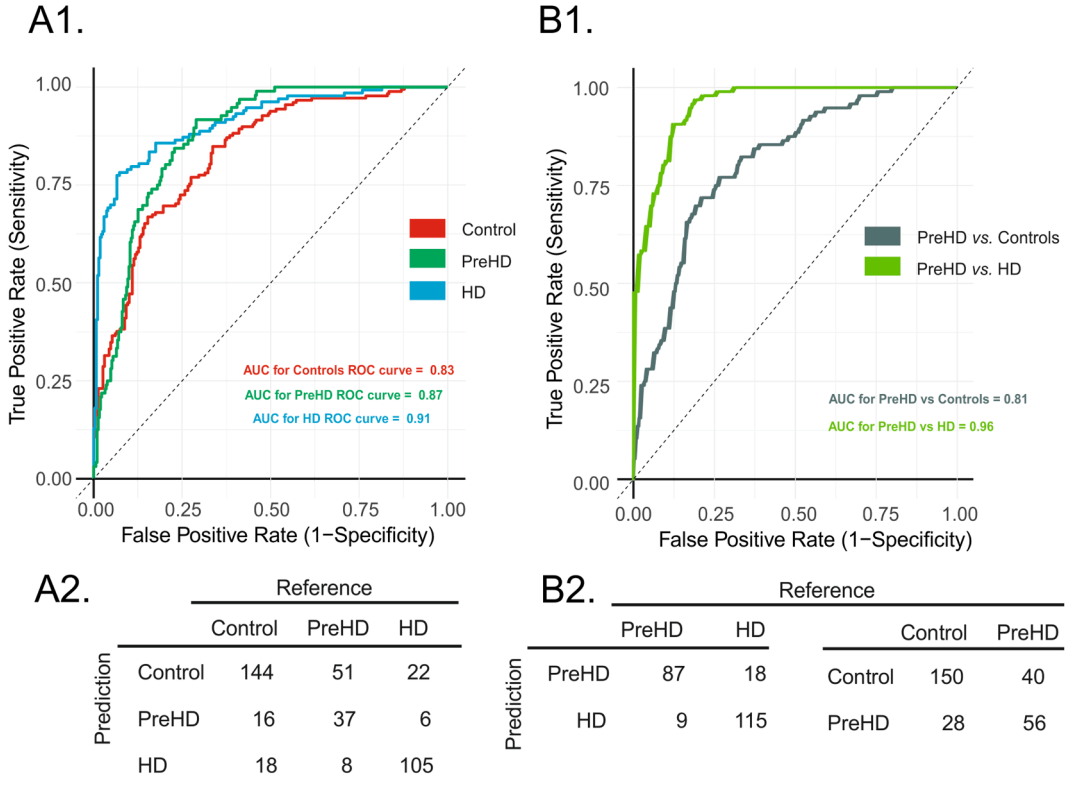

Fig. 5. Machine Learning Models evaluating MRI metrics as biomarkers. ROC-AUC curves and confusion matrices for classification performance **(A1)** SVMR model without RFE, including three subgroups (controls, PreHD, and HD); **(A2)** corresponding confusion matrix; **(B1)** SVMR models with RFE for classification in two scenarios, PreHD vs. controls, and PreHD vs. HD; **(B2)** corresponding confusion matrices. HD: symptomatic patients; PreHD: presymptomatic individuals; RFE: recursive feature elimination; SVMR: support vector machine model with radial basis function kernel.

Table 4
Statistics of the machine learning models obtained from tests datasets of the along-the-tract MRI metrics of both ATR in the scenario of presymptomatic subjects vs controls (A) and presymptomatic subjects vs symptomatic patients (B).

	Accuracy	Kappa	Sensitivity	Specificity	Precision	Recall	F1-score	AUC
A. Presymptomatic Subjects (positive class) vs Controls								
LBR without RFE	0.613	0.112	0.354	0.753	0.436	0.354	0.391	0.610
LBR with RFE	0.661	0.186	0.333	0.837	0.525	0.333	0.408	0.677
QDA without RFE	0.723	0.322	0.385	0.904	0.685	0.385	0.493	0.679
QDA with RFE	0.675	0.213	0.333	0.860	0.561	0.333	0.418	0.639
SVMR without RFE	0.737	0.394	0.521	0.854	0.658	0.521	0.581	0.821
SVMR with RFE	0.752	0.439	0.583	0.843	0.667	0.583	0.622	0.813
B. Presymptomatic Subjects (positive class) vs Symptomatic Patients								
LBR without RFE	0.738	0.463	0.698	0.767	0.684	0.698	0.691	0.798
LBR with RFE	0.725	0.431	0.646	0.782	0.681	0.646	0.663	0.793
QDA without RFE	0.738	0.476	0.781	0.707	0.658	0.781	0.714	0.836
QDA with RFE	0.751	0.505	0.823	0.699	0.664	0.823	0.735	0.823
SVMR without RFE	0.860	0.716	0.875	0.850	0.808	0.875	0.840	0.943
SVMR with RFE	0.882	0.761	0.906	0.865	0.829	0.906	0.866	0.958

AUC: area under the curve; LBR: logistic boost regression, QDA: quadratic discriminant analysis; RFE: recursive feature elimination; SVMR: support vector machines with radial basis function kernel.

scenarios. The ROC-AUC curves with the corresponding confusion matrices for the SVMR models with RFE for these two scenarios are shown in Fig. 5B.

4. Discussion

The present study aims to examine the ATR neurodegeneration in HD gene carriers by using a cross-sectional multimodal approach, combining WM microstructure and iron deposits evaluated by DTI and quantitative relaxometry, respectively. By integrating along-the-tract analyses with machine learning models, we provide new insights of the ATR involvement in HD across disease stages.

Regarding ATR microstructure, significant bilateral differences were observed in both premanifest and manifest HD groups compared to controls. In particular, in accordance with previous literature (Bourbon-Teles et al., 2019; Estevez-Fraga et al., 2021; Gregory et al., 2019; Odish et al., 2015; Phillips et al., 2014; Rosas et al., 2018; Saba et al., 2017), manifest HD patients exhibited microstructural alterations in both ATR, evidenced by higher average values in MD, RD, and AD compared to controls and premanifest individuals. These group differences extended beyond average metrics, with along-the-tract assessments showing the same results but also revealing a bilateral decrease in FA compared to premanifest individuals. Although standard diffusion metrics, as the ones reported here are not specific in terms of the underlying neural mechanisms, previous research suggests that such microstructural alteration could result from a combination of myelin disintegration, chronic axonal injury, axonal loss and/or ongoing inflammation (Aung et al., 2013; Ferrari Bardile et al., 2023; Field et al., 2024; Gatto et al., 2020; Jia et al., 2022; Li and Conforti, 2013; Pérot et al., 2024; Sun et al., 2022; Winklewski et al., 2018). This is supported by observed bilateral increases in both average and along-the-tract RD and AD values, as proxies of alterations in myelin integrity and axonal loss, respectively (Aung et al., 2013; Winklewski et al., 2018). Notably, the degeneration of both ATR in manifest patients was asymmetrical being more severe in the right ATR given the higher along-the-tract right-left differences in MD, RD and AD compared to controls and premanifest individuals. Specifically, the assessment of right-left asymmetries demonstrated differential physiological traits in gene carriers and healthy controls consisting of a reduced integrity of the right ATR as depicted by increased along-the-tract MD and AD compared to the left ATR, and this asymmetry was accentuated in manifest patients. Thus, this difference in integrity might confer a different susceptibility to huntingtin pathogenesis with an increased vulnerability of the right ATR to pathology (Lubben et al., 2021). This susceptibility has been also proven in other diseases, such as schizophrenia (Mamah et al., 2010).

In premanifest individuals, no significant differences were observed in average DTI or relaxometry values compared to healthy controls. However, the along-the-tract analysis revealed a previously unreported increase in white matter integrity within both ATRs, characterized by bilateral increases in FA accompanied by decreases in RD. Post-hoc pairwise permutation tests controlling for age suggested that these FA increases were more likely attributable to disease-related processes rather than age differences, as the increases were also observed in older individuals. Likewise, post-hoc pairwise permutation tests controlling for gender indicated that the observed FA increases could not be solely explained by the higher proportion of women in the presymptomatic group, as differences remained evident when comparing female participants alone. However, the possibility of similar FA increases in presymptomatic males could not be fully assessed due to the limited male representation in our sample, underscoring the need for further research in more gender-balanced samples.

The observed FA increases in presymptomatic individuals may reflect an early compensatory reorganization mechanism within the ATRs, potentially reflecting changes in structural connectivity prior to overt degeneration. The observed increase in FA and decrease in RD could point to alterations in myelin organization or other factors that contribute to enhanced axonal integrity, such as an increase in oligodendrocyte density as a neurodevelopmental effect of mHtt in the morphogenesis of the brain (Casella et al., 2022; Ferrari Bardile et al., 2023; Gomez-Tortosa et al., 2001) or a thickness increase in myelin sheath, as inferred from RD reductions and supported by early-stage increases in magnetization transfer, a proxy for myelin content (Winklewski et al., 2018; Pérot et al., 2024). This hypothesis is further supported by MR spectroscopy studies in HD mouse models showing early increases in choline and N-acetylaspartate (NAA), which have been interpreted as markers of compensatory mechanisms (Pérot et al., 2024). Alternatively, these changes might indicate a neuroplastic response, where the brain attempts to compensate neuronal dysfunction for ongoing pathological processes (Estevez-Fraga et al., 2021; Papoutsi et al., 2014; Pérot et al., 2024). In this regard, aligned studies have identified enhanced functional connectivity between the striatum and prefrontal cortex in premanifest HD patients, especially in the middle frontal areas and the anterior regions of the executive control network centred in the dorsolateral prefrontal cortex (Kronenbuerger et al., 2019; Werner et al., 2014; Wolf et al., 2014). In these studies, they have speculated that the enhanced functional connectivity of the striatum-prefrontal circuit could be indicating a compensatory mechanism to subserve functions that are affected. Moreover, a neuroinflammatory component in the left ATR cannot be excluded, as indicated by a left along-the-tract increase in AD, potentially indicating axonal repair with

microglial proliferation (Field et al., 2024; Gatto et al., 2020; Jia et al., 2022; Winklewski et al., 2018). In this sense, an increased AD in the ATR has been associated with circulating Th17 cells in bipolar disorder (Aronica et al., 2022), which could support the inflammatory theory.

Diverging findings compared to our results have also been reported in presymptomatic stages. For instance, Phillips et al., 2014 described an increase in average RD and AD in both ATR, while Rosas et al., 2018 found an increase in average RD exclusively in the right ATR in presymptomatic individuals near disease onset. These results were interpreted as early signs of ATR degeneration, suggesting that the ATR may be particularly vulnerable to early disruption in HD. Such discrepancies could stem from differences in sample characteristics, particularly related to the estimated years to onset, and methodological differences, such as the assessment of along-the-tract values and the use of non-parametric mathematical analysis in our study. Altogether, all these hypothesised physio-pathological mechanisms inferred by our findings should be further investigated to better understand the biological mechanisms associated to the pathology of ATR in HD.

Concerning iron levels, the right-left asymmetry assessment revealed a consistent along-the-tract R2* increase in the left ATR compared to the right ATR, a pattern that appeared to be a constitutional physiological trait, common to both gene carriers and healthy controls. Differences in iron levels amongst subgroups were observed exclusively in the along-the-tract R2* values. Premanifest individuals exhibited a bilateral asymmetrical R2* increase when compared to healthy controls and symptomatic patients, with the left ATR showing a more pronounced R2* increase. In manifest patients, R2* increase was detected only in the left ATR compared to controls. While average R2* increase in the left ATR has been previously reported in presymptomatic individuals compared to manifest patients (Phillips et al., 2014), little is known about R2* increase in manifest patients with no reports found describing it.

Our findings suggest that iron accumulation may begin early in the disease course, with a more significant impact on the left ATR. Physiopathologically, iron overload in HD has been linked to an up-regulation mediated by mutant huntingtin (mHTT) of iron regulation protein-1 (IRP1) and transferrin receptor (TfR) (Niu et al., 2018). Furthermore, histopathologically, two different potential mechanisms have been proposed. On one hand, the increased density in oligodendrocytes described in postmortem brains of presymptomatic carriers long before the expected onset of the clinical phenotype (Gomez-Tortosa et al., 2001) and remaining relatively stable with disease progression in animal models (Blockx et al., 2012b, 2012a; Ferrari Bardile et al., 2023) could interplay a role in this iron accumulation given that these cells are those with the highest iron concentration in the brain (Connor and Menzies, 1996; LeVine and Macklin, 1990). On the other hand, the ferric iron and ferritin accumulation has been detected in dystrophic microglia (Simmons et al., 2007), visible in all histological grades of Vonsattel (from 0 to 4), as part of the chronic neuroinflammation present in HD that contributes to neurodegeneration and further influences disease progression (Kempuraj et al., 2016; Thomsen et al., 2015). In this regard, mice HD models studied by MR spectroscopy have expressed an increase in glutamine at early stages remaining elevated at later stages related to astrocytic reactivity in an inflammatory background favouring the inflammatory hypothesis (Pérot et al., 2024).

Besides, the along-the-tract R2* decrease disclosed for the right ATR of manifest patients compared to healthy controls could be secondary to the further degeneration of the right ATR that might cause reductions of the relaxometry values, thereby limiting the ability to detect the R2* increase expected by the disease physiopathology (Phillips et al., 2014; Sánchez-Castañeda et al., 2015; Van Bergen et al., 2016). This hypothesis is supported by the explored correlations between relaxometry and diffusion tensor metrices, which could rely on the interrelated physical basis of both sequences. Specifically, the negative moderate correlations between relaxometry and diffusivities and the positive weak correlation between relaxometry and FA showed that reduced FA and increased diffusivities seen in manifest patients correlated with reduced relaxometry.

To gain a clearer insight into the interplay between iron alterations and microstructural changes, a correlation analysis between relaxometry values and diffusion tensor metrics was performed. We observed a positive correlation between white matter integrity and relaxometry values across the three groups (controls, premanifest and HD patients), suggesting an association between WM integrity and iron content. However, these findings not necessarily imply causality, that is, one factor may not directly result as a consequence of the other. For instance, in presymptomatic stages, it seems plausible that iron metabolism disruption associated with iron accumulation (Niu et al., 2018) along with an increase in oligodendrocyte density (Ferrari Bardile et al., 2023; Gomez-Tortosa et al., 2001) are synchronous processes, independent in nature, but partially interdependent in this early stage as oligodendrocytes are the CNS cell with the highest iron content (Connor and Menzies, 1996; LeVine and Macklin, 1990). Moreover, the negative correlation between relaxometry and RD supports the possibility that increased iron content might be associated with greater oligodendrocyte density, as reflected by a decrease in RD, which is considered a proxy of increased myelin integrity. In contrast, in symptomatic stages, the iron accumulation in the left ATR probably secondary to disruptions in iron metabolism (Niu et al., 2018) could potentially be synchronous with myelin loss linked to intrinsic oligodendroglial cell deficits driven by mHtt (Ferrari Bardile et al., 2023) and with axonal loss driven by huntingtin aggregates (Li et al., 2001). The ability to determine the relationship between iron and WM microstructure is limited in the right ATR of symptomatic patients by the fact that the increases in diffusivities and the decreases in fractional anisotropy and relaxometry values could reflect the same histological issue, namely a loss in WM integrity, as explained previously. In addition, iron's role in processes such as oxidative stress, ferroptosis (Berg and Youdim, 2006; Latunde-Dada, 2017; Manoharan et al., 2016; Mi et al., 2019; Wu et al., 2018) and chronic neuroinflammation (Kempuraj et al., 2016; Thomsen et al., 2015) could further contribute to the degeneration of the ATR in manifest patients. Nevertheless, while these observations point to a complex relationship between iron accumulation and WM microstructure, further studies are needed to better understand the coupling between these two processes.

Methodologically, the along-the-tract analysis was more sensitive to detect ATR anomalies in premanifest individuals, to identify subgroup differences regarding relaxometry values and to reveal laterality asymmetries and differences. This approach, previously applied to assess callosal integrity (Rosas et al., 2010), demonstrated similar enhanced sensitivity by revealing information that might be lost when examining tract means alone. Averaging DTI measures can blur part of the effects, adding the along-tract approach additional details (Shirazi et al., 2021). Microstructural properties vary along the length of a tract, showing localized sensitivity due to complex fiber configurations, such as dispersion, crossing fibers, and proximity to cerebrospinal fluid or gray matter, all of which can impact DTI metrics and relaxometry values (Hua et al., 2008; Pierpaoli and Basser, 1996; Szczepankiewicz et al., 2013).

Clinically, alterations in diffusion and iron-related microstructural properties of ATRs were significantly associated with clinical features of HD, supporting their involvement in disease progression, cognitive impairment, and psychiatric disturbances.

Regarding disease progression, CAP score, a proxy of disease burden, was significantly positively associated with both MD and RD of the right and left ATRs. Additionally, UHDRS functional scores showed significant negative associations with MD of the right ATR and RD of both ATRs. These findings suggest a bilateral, progressive disorganization of ATR white matter with advancing disease, reflecting a loss of microstructural integrity due to neurodegenerative processes, clinically translated into poorer global functioning.

In relation to cognition, both MD and RD of the right and left ATRs demonstrated significant negative correlations with UHDRS-cognitive

scores as well as Stroop interference performance. In addition, relaxometry values of the left ATR were significantly negatively associated with Stroop interference scores. Together, these results suggest a structural compromise in both ATRs associated with deficits in cognitive flexibility, and in executive and attention functions, in accordance with previous literature (Harrington et al., 2016; Matsui et al., 2015; Rosas et al., 2018) and further supporting the central role of the ATR in thalamo-cortical circuits underpinning cognitive control in HD.

Regarding psychiatric symptoms, apathy scores showed significant negative correlations with FA of both ATRs and with R2* relaxometry of the right ATR, indicating that reduced microstructural integrity and lower iron content in these regions are associated with increased apathetic symptoms. These findings suggest that the ATR, particularly the right hemisphere, plays a critical role in motivational regulation, consistent with previous studies linking fronto-thalamic disruption to apathy (Coenen et al., 2012; De Paepe et al., 2025, 2019;Torso et al., 2015). Interestingly, whereas the iron accumulation in the right ATR could be protective for apathy, iron accumulation in the left ATR could be detrimental to cognition in agreement with previous literature underlining the poorer cognitive performance in iron accumulation (Ferreira et al., 2019; Kalpouzos et al., 2017; Spence et al., 2020; Zachariou et al., 2020). Moreover, psychosis scores correlated negatively with RD of both ATRs, and irritability scores with MD of the right ATR, which may indicate a predisposition to these symptoms driven by aberrant compensatory white matter changes or coexisting inflammatory processes, both potentially associated with early stages of HD.

Concerning the assessment of DTI metrics and relaxometry as potential diagnostic biomarkers in HD, machine learning models demonstrated strong capabilities for classifying disease stages and identifying presymptomatic individuals, specially the SVMR models which obtained the highest performance in terms of confusion matrix derived metrices. Notably, the SVMR models with RFE excelled in differentiating presymptomatic from symptomatic patients and from controls, achieving high accuracies (88.2 % and 75.2 %, respectively) and underscoring the importance of including these parameters to understand and characterize disease stages. These findings underscore the interplay between WM integrity and iron levels as sensitive indicators of neurodegeneration, reflecting early structural and biochemical brain changes.

There are different limitations to consider in this study. The cross-sectional design restricts our ability to track the temporal progression of ATR neurodegeneration. Longitudinal studies with larger and more demographically balanced cohorts are required to validate these findings and better characterize disease-related changes over time. For example, although gender differences between presymptomatic participants and controls were statistically controlled in the models by including gender as a covariate, and further assessed in post hoc analyses, the overrepresentation of females in the presymptomatic group may result in a limited extensibility of the results in males. This is especially relevant given the well-documented sex-related variability in white matter microstructure (Herlin et al., 2024). In addition, although age differences between presymptomatic participants and controls were not statistically significant, the presymptomatic group was on average 6 years younger. To address this potential confound, age was also included as a covariate in the statistical models. Furthermore, post-hoc analysis were conducted to evaluate ATR integrity across different ages groups. These analyses indicated that the observed FA increases were not attributable to the younger age of presymptomatic individuals, supporting the interpretation that these changes are disease-related rather than solely age-driven. Nevertheless, future studies should aim to recruit more demographically matched samples to further minimize potential confounding effects and enhance the generalizability of the findings.

Another limitation is the inherent lack of specificity in DTI, which makes it challenging to distinguish between coexisting pathologies such as inflammation, demyelination, axonal loss and injury. DTI metrics can underestimate the extent of demyelination and to overestimate axonal injury, reducing their specificity in contexts where multiple pathological processes are present (Wheeler-Kingshott and Cercignani, 2009; Winklewski et al., 2018). Additionally, although relaxometry is often used as an indicator of iron content, it has limitations due to its lack of specificity. As a T2*-weighted gradient-echo sequence, the signal is influenced not only by substances that affect magnetic susceptibility, such as iron, blood products and calcium, but also by other tissue characteristics, including myelination and water content. Specifically, an increase in iron levels results in R2* increase, while tissue damage associated with increased water and demyelination results in a decrease in R2* measurements (Phillips et al., 2014; Van Bergen et al., 2016). Thus, relaxometry has the inherent limitation in differentiating between these two concomitant histopathological processes often presented in neurodegenerative diseases (Berg and Youdim, 2006; Simmons et al., 2007; Wu et al., 2018), but combining relaxometry measures with diffusivity metrics can yield a more comprehensive understanding of the underlying pathology, being highly recommendable to consider the changes in relaxometry values alongside the changes in WM integrity. Future neuropathological studies are needed involving datasets to confirm and expand upon our findings. Lastly, a key limitation of the machine learning models lies in the assumption of independence among along-the-tract values. Since each individual contributes multiple spatially adjacent measurements along the tract, these observations are inherently correlated. Treating them as independent during model training and testing may overestimate model performance estimates. Future research should consider implementing modelling strategies that explicitly account for within-subject spatial dependencies to enhance robustness and generalizability of predictive models.

In conclusion, alterations in ATR microstructure and iron dysregulation take place across both premanifest and manifest stages of HD, potentially reflecting a metachronous pattern: the initial iron increase persisted across both disease stages, while white matter degeneration became evident in the manifest stage, potentially intensified by iron toxicity. Both ATRs are critically involved in mediating core clinical features of HD, including disease progression, cognitive dysfunction, and neuropsychiatric symptoms. Moreover, relaxometry values and DTI metrics of both ATR show promises in tested machine-learning models for accurately distinguishing disease stages, particularly in identifying presymptomatic individuals from both healthy controls and symptomatic patients. Nevertheless, further refinement and inclusion of additional metrics are needed to enhance the diagnostic performance of these models. Overall, our findings highlight the ATR as a key region of early vulnerability and progressive degeneration in HD, and underscore iron accumulation as a potentially important driver of white matter pathology. These insights warrant further longitudinal and multimodal investigations to better understand the mechanistic interplay between iron and white matter changes and to support biomarker development for early detection and disease monitoring in HD.

Funding statement

This work was supported by the Instituto de Salud Carlos III, which is an agency of the MCI, co-funded by FEDER funds/European Regional Development Fund (ERDF) – a way to Build Europe (CP13/00225, PI14/00834, to EC). This study was also funded by AGAUR 2021SGR00352, the Agencia Estatal de Investigación (AEI), an agency of MCI, and co-funded by FEDER funds/European Regional Development Fund (ERDF) – a Way to Build Europe (number PID2020-114518RB-I00 / DOI: 10.13039/501100011033 to EC). We also thank CERCA Programme/Generalitat de Catalunya for institutional support.

Declaration of Generative AI and AI-assisted technologies in the writing process

During the preparation of this work, the author(s) used ChatGPT (version 4) to assist with language and grammar correction. After using this tool, the author(s) reviewed and edited the content as needed and

take(s) full responsibility for the final version of the publication.

CRediT authorship contribution statement

Montserrat Domingo-Ayllón: Writing – review & editing, Writing – original draft, Validation, Investigation, Formal analysis, Data curation, Conceptualization. **Clara Garcia-Gorro:** Writing – review & editing, Data curation. **Nadia Rodriguez-Dechicha:** Writing – review & editing, Data curation. **Irene Vaquer:** Writing – review & editing, Data curation. **Matilde Calopa:** Writing – review & editing, Data curation. **Ruth de Diego-Balaguer:** Writing – review & editing, Resources, Funding acquisition, Data curation. **Estela Camara:** Writing – review & editing, Supervision, Resources, Project administration, Investigation, Funding acquisition, Data curation, Conceptualization.

Declaration of competing interest

The authors declare that they have no known competing financial interests or personal relationships that could have appeared to influence the work reported in this paper.

Acknowledgements

The authors are grateful to the patients and their families for their participation in this project. We would also like to thank Dr. Saül Martinez-Horta, Dr. Jesús Pérez Pérez, Dr. Jaime Kulisevksy, Pilar Sanchez, Dr. Esteban Muñoz, Celia Mareca and Dr. Ruiz-Idiago for help with clinical evaluation.

Appendix A. Supplementary data

Supplementary data to this article can be found online at https://doi.org/10.1016/j.nicl.2025.103866.

Data availability

The raw data that supports the findings of this study are available from the corresponding author upon reasonable request after approval of local institutional review board.

References

Aronica, R., Enrico, P., Squarcina, L., Brambilla, P., Delvecchio, G., 2022. Association between Diffusion Tensor Imaging, inflammation and immunological alterations in unipolar and bipolar depression: a review. Neurosci. Biobehav. Rev. 143, 104922. https://doi.org/10.1016/j.neubiorev.2022.104922.

Aung, W.Y., Mar, S., Benzinger, T.L., 2013. Diffusion tensor MRI as a biomarker in axonal and myelin damage. Imaging Med 5, 427–440. https://doi.org/10.2217/iim.13.49.

Aylward, E.H., Nopoulos, P.C., Ross, C.A., Langbehn, D.R., Pierson, R.K., Mills, J.A., Johnson, H.J., Magnotta, V.A., Juhl, A.R., Paulsen, J.S., 2011. Longitudinal change in regional brain volumes in prodromal Huntington disease. J. Neurol. Neurosurg. Psychiatry 82, 405–410. https://doi.org/10.1136/jnnp.2010.208264.

Aylward, E.H., Sparks, B.F., Field, K.M., Yallapragada, V., Shpritz, B.D., Rosenblatt, A., Brandt, J., Gourley, L.M., Liang, K., Zhou, H., Margolis, R.L., Ross, C.A., 2004. Onset and rate of striatal atrophy in preclinical Huntington disease. Neurology 63, 66–72. https://doi.org/10.1212/01.WNL.0000132965.14653.D1.

Bano, D., Zanetti, F., Mende, Y., Nicotera, P., 2011. Neurodegenerative processes in Huntington's disease. Cell Death Dis. 2, 1–7. https://doi.org/10.1038/cddis.2011.112.

Bardile, C.F., Garcia-Miralles, M., Caron, N.S., Rayan, N.A., Langley, S.R., Harmston, N., Rondelli, A.M., Yi Teo, R.T., Waltl, S., Anderson, L.M., Bae, H.G., Jung, S., Williams, A., Prabhakar, S., Petretto, E., Hayden, M.R., Pouladi, M.A., 2019. Intrinsic mutant HTT-mediated defects in oligodendroglia cause myelination deficits and behavioral abnormalities in Huntington disease. PNAS 116, 9622–9627. https://doi.org/10.1073/PNAS.1818042116/-/DCSUPPLEMENTAL.

Baudrexel, S., Volz, S., Preibisch, C., Klein, J.C., Steinmetz, H., Diger Hilker, R., Deichmann, R., 2009. Rapid Single-Scan T * 2-Mapping using Exponential Excitation Pulses and Image-based Correction for Linear Background Gradients. Magn. Reson. Med. https://doi.org/10.1002/mrm.21971.

Berg, D., Youdim, M.B.H., 2006. Role of iron in neurodegenerative disorders. Top. Magn. Reson. Imaging 17, 5–17. https://doi.org/10.1097/01.rmr.0000245461.90406.ad.

Blockx, I., De Groof, G., Verhoye, M., Van Audekerke, J., Raber, K., Poot, D., Sijbers, J., Osmand, A.P., Von Hörsten, S., Van der Linden, A., 2012. Microstructural changes observed with DKI in a transgenic Huntington rat model: evidence for abnormal neurodevelopment. Neuroimage 59, 957–967. https://doi.org/10.1016/j.neuroimage.2011.08.062.

Blockx, I., Verhoye, M., Van Audekerke, J., Bergwerf, I., Kane, J.X., Delgado y Palacios, R., Veraart, J., Jeurissen, B., Raber, K., von Hörsten, S., Ponsaerts, P., Sijbers, J., Leergaard, T.B., Van der Linden, A., 2012b. Identification and characterization of Huntington related pathology: An in vivo DKI imaging study. Neuroimage 63, 653–662. https://doi.org/10.1016/j.neuroimage.2012.06.032.

Blumenstock, S., Dudanova, I., 2020. Cortical and Striatal Circuits in Huntington's Disease. Front. Neurosci. 14. https://doi.org/10.3389/fnins.2020.00082.

Bourbon-Teles, J., Bells, S., Jones, D.K., Coulthard, E., Rosser, A., Metzler-Baddeley, C., 2019. Myelin Breakdown in Human Huntington's Disease: Multi-Modal evidence from Diffusion MRI and Quantitative Magnetization transfer. Neuroscience 403, 79–92. https://doi.org/10.1016/j.neuroscience.2017.05.042.

Casella, C., Chamberland, M., Laguna, P.L., Parker, G.D., Rosser, A.E., Coulthard, E., Rickards, H., Berry, S.C., Jones, D.K., Metzler-Baddeley, C., 2022. Mutation-related magnetization-transfer, not axon density, drives white matter differences in premanifest Huntington disease: evidence from in vivo ultra-strong gradient MRI. Hum. Brain Mapp. 43, 3439–3460. https://doi.org/10.1002/HBM.25859.

Casella, C., Lipp, I., Rosser, A., Jones, D.K., Metzler-Baddeley, C., 2020. A critical Review of White Matter changes in Huntington's Disease. Mov. Disord. 35, 1302–1311. https://doi.org/10.1002/MDS.28109.

Cho, Z.H., Law, M., Chi, J.G., Choi, S.H., Park, S.Y., Kammen, A., Park, C.W., Oh, S.H., Kim, Y.B., 2015. An anatomic review of thalamolimbic fiber tractography: Ultra-high resolution direct visualization of thalamolimbic fibers anterior thalamic radiation, superolateral and inferomedial medial forebrain bundles, and newly identified septum pellucidum tract. World Neurosurg. 83 (54–61), E32. https://doi.org/10.1016/j.wneu.2013.08.022.

Coenen, V.A., Panksepp, J., Hurwitz, T.A., Urbach, H., Mädler, B., 2012. Human Medial Forebrain Bundle (MFB) and Anterior Thalamic Radiation (ATR): Imaging of two Major Subcortical Pathways and the Dynamic Balance of Opposite Affects in Understanding Depression. J. Neuropsychiatry Clin. Neurosci. 24, 223–236. https://doi.org/10.1176/appi.neuropsych.11080180.

Connor, J.R., Menzies, S.L., 1996. Relationship of iron to oligondendrocytes and myelination. Glia 17, 83–93. https://doi.org/10.1002/(SICI)1098-1136(199606)17:2<83::AID-GLIA1>3.0.CO;2-7.

Craufurd, D., Thompson, J.C., Snowden, J.S., 2001. Behavioral changes in Huntington Disease. Neuropsychiatry Neuropsychol. Behav. Neurol. 219–226.

Della Nave, R., Ginestroni, A., Tessa, C., Giannelli, M., Piacentini, S., Filippi, M., Mascalchi, M., 2010. Regional distribution and clinical correlates of white matter structural damage in Huntington disease: a tract-based spatial statistics study. Am. J. Neuroradiol. 31, 1675–1681. https://doi.org/10.3174/ajnr.A2128.

De Paepe, A.E., Bikou, V., Turan, E., Pérez-Bellido, A., Garcia-Gorro, C., Rodriguez-Dechicha, N., Vaquer, I., Calopa, M., de Diego-Balaguer, R., Camara, E., 2025. Striato-cortical connectivity patterns predict clinical profiles in Huntington's disease. Neuroimage Clin 46, 103788. https://doi.org/10.1016/j.nicl.2025.103788.

De Paepe, A.E., Sierpowska, J., Garcia-Gorro, C., Martinez-Horta, S., Perez-Perez, J., Kulisevsky, J., Rodriguez-Dechicha, N., Vaquer, I., Subira, S., Calopa, M., Muñoz, E., Santacruz, P., Ruiz-Idiago, J., Mareca, C., de Diego-Balaguer, R., Camara, E., 2019. White matter cortico-striatal tracts predict apathy subtypes in Huntington's disease. Neuroimage Clin 24, 101965. https://doi.org/10.1016/j.nicl.2019.101965.

Domínguez D, J.F., Egan, G.F., Gray, M.A., Poudel, G.R., Churchyard, A., Chua, P., Stout, J.C., Georgiou-Karistianis, N., 2013. Multi-Modal Neuroimaging in Premanifest and Early Huntington's Disease: 18 Month Longitudinal Data from the IMAGE-HD Study. PLoS One 8, e74131. https://doi.org/10.1371/journal.pone.0074131.

Enroll-HD, n.d. Enroll-HD-PDS6: Understand and Interpret the Data | 2022-12-22.

Estevez-Fraga, C., Scahill, R., Rees, G., Tabrizi, S.J., Gregory, S., 2021. Diffusion imaging in Huntington's disease: comprehensive review Movement disorders. J. Neurol. Neurosurg. Psychiatry 92, 62–69. https://doi.org/10.1136/jnnp-2020-324377.

Fama, R., Sullivan, E.V., 2015. Thalamic structures and associated cognitive functions: Relations with age and aging. Neurosci. Biobehav. Rev. 54, 29–37. https://doi.org/10.1016/j.neubiorev.2015.03.008.

Faria, A.V., Ratnanather, J.T., Tward, D.J., Lee, D.S., Van Den Noort, F., Wu, D., Brown, T., Johnson, H., Paulsen, J.S., Ross, C.A., Younes, L., Miller, M.I., 2016. Linking white matter and deep gray matter alterations in premanifest Huntington disease. Neuroimage Clin 11, 450–460. https://doi.org/10.1016/j.nicl.2016.02.014.

Ferrari Bardile, C., Radulescu, C.I., Pouladi, M.A., 2023. Oligodendrocyte pathology in Huntington's disease: from mechanisms to therapeutics. Trends Mol. Med. 29, 802–816. https://doi.org/10.1016/j.molmed.2023.07.010.

Ferreira, A., Neves, P., Gozzelino, R., 2019. pharmaceuticals Multilevel Impacts of Iron in the Brain: the Cross talk between Neurophysiological Mechanisms. Cognition, and Social Behavior. https://doi.org/10.3390/ph12030126.

Field, S.E., Curle, A.J., Barker, R.A., 2024. Inflammation and Huntington's disease – a neglected therapeutic target? Expert Opin. Invest. Drugs 33, 451–467. https://doi.org/10.1080/13543784.2024.2348738.

Furlong, L.S., Jakabek, D., Power, B.D., Owens-Walton, C., Wilkes, F.A., Walterfang, M., Velakoulis, D., Egan, G., Looi, J.C., Georgiou-Karistianis, N., 2020. Morphometric in vivo evidence of thalamic atrophy correlated with cognitive and motor dysfunction in Huntington's disease: the IMAGE-HD study. Psychiatry Res. Neuroimaging 298. https://doi.org/10.1016/j.pscychresns.2020.111048.

Gatto, E.M., Rojas, N.G., Persi, G., Etcheverry, J.L., Cesarini, M.E., Perandones, C., 2020. Huntington disease: advances in the understanding of its mechanisms. Clin Park Relat Disord 3, 100056. https://doi.org/10.1016/j.prdoa.2020.100056.

Gomez-Tortosa, E., MacDonald, M.E., Friend, J.C., Taylor, S.A.M., Weiler, L.J., Adrienne Cupples, L., Srinidhi, J., Gusella, J.F., Bird, E.D., Vonsattel, J.P., Myers, R.H., 2001. Quantitative neuropathological changes in presymptomatic Huntington's disease.

Ann. Neurol. 49, 29–34. https://doi.org/10.1002/1531-8249(200101)49:1<29::AID-ANA7>3.3.CO;2-2.
Gregory, S., Johnson, E., Byrne, L.M., Rodrigues, F.B., Henderson, A., Moss, J., Thomas, D., Zhang, H., De Vita, E., Tabrizi, S.J., Rees, G., Scahill, R.I., Wild, E.J., 2019. Characterizing White Matter in Huntington's Disease. https://doi.org/10.1002/mdc3.12866.
Greve, D.N., Fischl, B., 2009. Accurate and robust brain image alignment using boundary-based registration. Neuroimage 48, 63–72. https://doi.org/10.1016/j.neuroimage.2009.06.060.
Han, I., You, Y., Kordower, J.H., Brady, S.T., Morfini, G.A., 2010. Differential vulnerability of neurons in Huntington's disease: the role of cell type-specific features. J. Neurochem. https://doi.org/10.1111/j.1471-4159.2010.06672.x.
Harrington, D.L., Long, J.D., Durgerian, S., Mourany, L., Koenig, K., Bonner-Jackson, A., Paulsen, J.S., Rao, S.M., 2016. Cross-sectional and longitudinal multimodal structural imaging in prodromal Huntington's disease. Mov. Disord. 31, 1664–1675. https://doi.org/10.1002/mds.26803.
Herlin, B., Uszynski, I., Chauvel, M., Dupont, S., Poupon, C., 2024. Sex-related variability of white matter tracts in the whole HCP cohort. Brain Struct. Funct. 229, 1713–1735. https://doi.org/10.1007/s00429-024-02833-0.
Hua, K., Zhang, J., Wakana, S., Jiang, H., Li, X., Reich, D.S., Calabresi, P.A., Pekar, J.J., van Zijl, P.C.M., Mori, S., 2008. Tract probability maps in stereotaxic spaces: analyses of white matter anatomy and tract-specific quantification. Neuroimage 39, 336–347. https://doi.org/10.1016/j.neuroimage.2007.07.053.
Jankowski, M.M., Ronnqvist, K.C., Tsanov, M., Vann, S.D., Wright, N.F., Erichsen, J.T., Aggleton, J.P., O'Mara, S.M., 2013. The anterior thalamus provides a subcortical circuit supporting memory and spatial navigation. Front. Syst. Neurosci. 7, 1–12. https://doi.org/10.3389/fnsys.2013.00045.
Jia, Q., Li, S., Li, X.-J., Yin, P., 2022. Neuroinflammation in Huntington's disease: from animal models to clinical therapeutics. Front. Immunol. 13. https://doi.org/10.3389/fimmu.2022.1088124.
Kakou, M., Kouakou, F., N'dri Oka, D., Mbende, A.S., Peltier, J., Velut, S., 2017. Microanatomy of Thalamic Radiations. International Journal of Human Anatomy 1, 28–37. https://doi.org/10.14302/issn.2577-2279.ijha-17-1719.
Kalpouzos, G., Garzón, B., Sitnikov, R., Heiland, C., Salami, A., Persson, J., Bäckman, L., 2017. Higher Striatal Iron Concentration is Linked to Frontostriatal Underactivation and Poorer memory in Normal Aging. Cereb. Cortex 27, 3427–3436. https://doi.org/10.1093/cercor/bhx045.
Kempuraj, D., Thangavel, R., Natteru, P.A., Selvakumar, G.P., Saeed, D., Zahoor, H., Zaheer, S., Iyer, S.S., Zaheer, A., 2016. Neuroinflammation Induces Neurodegeneration. J Neurol Neurosurg Spine 1, 1–15.
Kronenbuerger, M., Hua, J., Bang, J.Y.A., Ultz, K.E., Miao, X., Zhang, X., Pekar, J.J., van Zijl, P.C.M., Duan, W., Margolis, R.L., Ross, C.A., 2019. Differential changes in Functional Connectivity of Striatum-Prefrontal and Striatum-Motor Circuits in Premanifest Huntington's Disease. Neurodegener Dis 19, 78–87. https://doi.org/10.1159/000501616.
Latunde-Dada, G.O., 2017. Ferroptosis: Role of lipid peroxidation, iron and ferritinophagy. Biochim. Biophys. Acta Gen. Subj. 1861, 1893–1900. https://doi.org/10.1016/j.bbagen.2017.05.019.
Leemans, A., Jones, D.K., 2009. The B-matrix must be rotated when correcting for subject motion in DTI data. Magn. Reson. Med. 61, 1336–1349. https://doi.org/10.1002/mrm.21890.
LeVine, S.M., Macklin, W.B., 1990. Iron-enriched oligodendrocytes: a reexamination of their spatial distribution. J. Neurosci. Res. 26, 508–512. https://doi.org/10.1002/jnr.490260415.
Li, H., Li, S.-H., Yu, Z.-X., Shelbourne, P., Li, X.-J., 2001. Huntingtin Aggregate-Associated Axonal Degeneration is an Early Pathological Event in Huntington's Disease mice. J. Neurosci. 21, 8473–8481. https://doi.org/10.1523/JNEUROSCI.21-21-08473.2001.
Li, J.-Y., Conforti, L., 2013. Axonopathy in Huntington's disease. Exp. Neurol. 246, 62–71. https://doi.org/10.1016/j.expneurol.2012.08.010.
Lubben, N., Ensink, E., Coetzee, G.A., Labrie, V., 2021. The enigma and implications of brain hemispheric asymmetry in neurodegenerative diseases. Brain Commun 3. https://doi.org/10.1093/braincomms/fcab211.
Mamah, D., Conturo, T.E., Harms, M.P., Akbudak, E., Wang, L., McMichael, A.R., Gado, M.H., Barch, D.M., Csernansky, J.G., 2010. Anterior thalamic radiation integrity in schizophrenia: a diffusion-tensor imaging study. Psychiatry Res. Neuroimaging 183, 144–150. https://doi.org/10.1016/j.pscychresns.2010.04.013.
Manoharan, S., Guillemin, G.J., Abiramasundari, R.S., Essa, M.M., Akbar, M., Akbar, M. D., 2016. The Role of Reactive Oxygen Species in the Pathogenesis of Alzheimer's Disease, Parkinson's Disease, and Huntington's Disease: a Mini Review. Oxid. Med. Cell. Longev. 2016. https://doi.org/10.1155/2016/8590578.
Martinez-Horta, S., Perez-Perez, J., van Duijn, E., Fernandez-Bobadilla, R., Carceller, M., Pagonabarraga, J., Pascual-Sedano, B., Campolongo, A., Ruiz-Idiago, J., Sampedro, F., Landwehrmeyer, G.B., Kulisevsky, J., 2016. Neuropsychiatric symptoms are very common in premanifest and early stage Huntington's Disease. Parkinsonism Relat. Disord. 25, 58–64. https://doi.org/10.1016/j.parkreldis.2016.02.008.
Matsui, J.T., Vaidya, J.G., Wassermann, D., Kim, R.E., Magnotta, V.A., Johnson, H.J., Paulsen, J.S., 2015. Prefrontal cortex white matter tracts in prodromal Huntington disease. Hum. Brain Mapp. 36, 3717–3732. https://doi.org/10.1002/hbm.22835.
McColgan, P., Seunarine, K.K., Razi, A., Cole, J.H., Gregory, S., Durr, A., Roos, R.A.C., Stout, J.C., Landwehrmeyer, B., Scahill, R.I., Clark, C.A., Rees, G., 2015. Selective vulnerability of Rich Club brain regions is an organizational principle of structural connectivity loss in Huntington's disease. Brain 138, 3327–3344. https://doi.org/10.1093/brain/awv259.
McColgan, P., Tabrizi, S.J., 2018. Huntington's disease: a clinical review. Eur. J. Neurol. https://doi.org/10.1111/ene.13413.
Mi, Y., Gao, X., Xu, H., Cui, Y., Zhang, Y., Gou, X., 2019. The Emerging Roles of Ferroptosis in Huntington's Disease. NeuroMol. Med. 21, 110–119. https://doi.org/10.1007/s12017-018-8518-6.
Mitchell, A.S., 2015. The mediodorsal thalamus as a higher order thalamic relay nucleus important for learning and decision-making. Neurosci. Biobehav. Rev. 54, 76–88. https://doi.org/10.1016/j.neubiorev.2015.03.001.
Montoya-Filardi, A., García-Junco Albacete, M., Ortolá Fortes, P., Carreres Polo, J., 2022. Carretera perdida: imagen de la degeneración neuronal secundaria. Radiologia 64, 145–155. https://doi.org/10.1016/j.rx.2022.01.008.
Muhoberac, B.B., Vidal, R., 2013. Abnormal iron homeostasis and neurodegeneration. Front. Aging Neurosci. 5. https://doi.org/10.3389/fnagi.2013.00032.
Muller, M., Leavitt, B.R., 2014. Iron dysregulation in Huntington's disease. J. Neurochem. 130, 328–350. https://doi.org/10.1111/jnc.12739.
Niccolini, F., 2014. Neuroimaging in Huntington's disease. World J. Radiol. 6, 301. https://doi.org/10.4329/wjr.v6.i6.301.
Niu, L., Ye, C., Sun, Y., Peng, T., Yang, S., Wang, W., Li, H., 2018. Mutant huntingtin induces iron overload via up-regulating IRP1 in Huntington's disease. Cell Biosci. 8, 1–12. https://doi.org/10.1186/s13578-018-0239-x.
Novak, M.J.U., Seunarine, K.K., Gibbard, C.R., Mccolgan, P., Draganski, B., Friston, K., Clark, C.A., Tabrizi, S.J., 2015. Basal ganglia-cortical structural connectivity in Huntington's disease. Hum. Brain Mapp. 36, 1728–1740. https://doi.org/10.1002/HBM.22733.
Odish, O.F.F., Leemans, A., Reijntjes, R.H.A.M., van den Bogaard, S.J.A., Dumas, E.M., Wolterbeek, R., Tax, C.M.W., Kuijf, H.J., Vincken, K.L., van der Grond, J., Roos, R.A. C., 2015. Microstructural brain abnormalities in Huntington's disease: a two-year follow-up. Hum. Brain Mapp. 36, 2061–2074. https://doi.org/10.1002/hbm.22756.
Papoutsi, M., Labuschagne, I., Tabrizi, S.J., Stout, J.C., 2014. The cognitive burden in Huntington's disease: Pathology, phenotype, and mechanisms of compensation. Mov. Disord. 29, 673–683. https://doi.org/10.1002/MDS.25864.
Pergola, G., Danet, L., Pitel, A.L., Carlesimo, G.A., Segobin, S., Pariente, J., Suchan, B., Mitchell, A.S., Barbeau, E.J., 2018. The Regulatory Role of the Human Mediodorsal Thalamus. Trends Cogn. Sci. 22, 1011–1025. https://doi.org/10.1016/j.tics.2018.08.006.
Pérot, J.-B., Brouillet, E., Flament, J., 2024. The contribution of preclinical magnetic resonance imaging and spectroscopy to Huntington's disease. Front. Aging Neurosci. 16. https://doi.org/10.3389/fnagi.2024.1306312.
Phillips, O., Squitieri, F., Sanchez-Castaneda, C., Elifani, F., Caltagirone, C., Sabatini, U., Di Paola, M., 2014. Deep white matter in Huntington's disease. PLoS One 9, 1–11. https://doi.org/10.1371/journal.pone.0109676.
Pierpaoli, C., Basser, P.J., 1996. Toward a quantitative assessment of diffusion anisotropy. Magn. Reson. Med. 36, 893–906. https://doi.org/10.1002/mrm.1910360612.
R Core Team, 2024. R: A language and Environment for Statistical Computing. R Foundation for Statistical Computing. Vienna, Austria. [WWW Document]. URL https://www.R-project.org/ (accessed 5.11.24).
Reiner, A., Dragatsis, I., Dietrich, P., 2011. Genetics and neuropathology of huntington's disease, in: International Review of Neurobiology. Academic Press Inc., pp. 325–372. https://doi.org/10.1016/B978-0-12-381328-2.00014-6.
Rosas, H.D., Lee, S.Y., Bender, A.C., Zaleta, A.K., Vangel, M., Yu, P., Fischl, B., Pappu, V., Onorato, C., Cha, J.H., Salat, D.H., Hersch, S.M., 2010. Altered white matter microstructure in the corpus callosum in Huntington's disease: Implications for cortical "disconnection. Neuroimage 49, 2995–3004. https://doi.org/10.1016/j.neuroimage.2009.10.015.
Rosas, H.D., Wilkens, P., Salat, D.H., Mercaldo, N.D., Vangel, M., Yendiki, A.Y., Hersch, S.M., 2018. Complex spatial and temporally defined myelin and axonal degeneration in Huntington disease. Neuroimage Clin 20, 236–242. https://doi.org/10.1016/j.nicl.2018.01.029.
Ross, C.A., Aylward, E.H., Wild, E.J., Langbehn, D.R., Long, J.D., Warner, J.H., Scahill, R. I., Leavitt, B.R., Stout, J.C., Paulsen, J.S., Reilmann, R., Unschuld, P.G., Wexler, A., Margolis, R.L., Tabrizi, S.J., 2014. Huntington disease: Natural history, biomarkers and prospects for therapeutics. Nat. Rev. Neurol. 10, 204–216. https://doi.org/10.1038/nrneurol.2014.24.
Saba, R.A., Yared, J.H., Doring, T.M., Borges, V., Ferraz, H.B., 2017. Diffusion tensor imaging of brain white matter in huntington gene mutation individuals. Arq. Neuropsiquiatr. 75, 503–508. https://doi.org/10.1590/0004-282x20170085.
Sánchez-Castañeda, C., Squitieri, F., Di Paola, M., Dayan, M., Petrollini, M., Sabatini, U., 2015. The role of iron in gray matter degeneration in huntington's disease: a magnetic resonance imaging study. Hum. Brain Mapp. 36, 50–66. https://doi.org/10.1002/hbm.22612.
Shirazi, Y., Oghabian, M.A., Batouli, S.A.H., 2021. Along-tract analysis of the white matter is more informative about brain ageing, compared to whole-tract analysis. Clin. Neurol. Neurosurg. 211, 107048. https://doi.org/10.1016/j.clineuro.2021.107048.
Simmons, D.A., Casale, M., Alcon, B., Pham, N., Narayan, N., Lynch, G., 2007. Ferritin accumulation in dystrophic microglia is an early event in the development of Huntington's disease. Glia 55, 1074–1084. https://doi.org/10.1002/glia.20526.
Spence, H., McNeil, C.J., Waiter, G.D., 2020. The impact of brain iron accumulation on cognition: a systematic review. PLoS One 15. https://doi.org/10.1371/journal.pone.0240697.
Stephenson, J., Nutma, E., van der Valk, P., Amor, S., 2018. Inflammation in CNS Neurodegenerative Diseases. Immunology 154, 204–219. https://doi.org/10.1111/imm.12922.
Stoffers, D., Sheldon, S., Kuperman, J.M., Goldstein, J., Corey-Bloom, J., Aron, A.R., 2010. Contrasting gray and white matter changes in preclinical Huntington disease:

an MRI study. Neurology 74, 1208–1216. https://doi.org/10.1212/WNL.0b013e3181d8c20a.
Sun, Y., Tong, H., Yang, T., Liu, L., Li, X.-J., Li, S., 2022. Insights into White Matter defect in Huntington's Disease. Cells 11, 3381. https://doi.org/10.3390/cells11213381.
Szczepankiewicz, F., Lätt, J., Wirestam, R., Leemans, A., Sundgren, P., van Westen, D., Ståhlberg, F., Nilsson, M., 2013. Variability in diffusion kurtosis imaging: Impact on study design, statistical power and interpretation. Neuroimage 76, 145–154. https://doi.org/10.1016/j.neuroimage.2013.02.078.
Tabrizi, S.J., Scahill, R.I., Owen, G., Durr, A., Leavitt, B.R., Roos, R.A., Borowsky, B., Landwehrmeyer, B., Frost, C., Johnson, H., Craufurd, D., Reilmann, R., Stout, J.C., Langbehn, D.R., 2013. Predictors of phenotypic progression and disease onset in premanifest and early-stage Huntington's disease in the TRACK-HD study: analysis of 36-month observational data. Lancet Neurol. 12, 637–649. https://doi.org/10.1016/S1474-4422(13)70088-7.
Thomsen, M.S., Andersen, M.V., Christoffersen, P.R., Jensen, M.D., Lichota, J., Moos, T., 2015. Neurodegeneration with inflammation is accompanied by accumulation of iron and ferritin in microglia and neurons. Neurobiol. Dis. 81, 108–118. https://doi.org/10.1016/j.nbd.2015.03.013.
Torso, M., Serra, L., Giulietti, G., Spanò, B., Tuzzi, E., Koch, G., Caltagirone, C., Cercignani, M., Bozzali, M., 2015. Strategic Lesions in the Anterior Thalamic Radiation and Apathy in Early Alzheimer's Disease. PLoS One 10, e0124998. https://doi.org/10.1371/journal.pone.0124998.
Van Bergen, J.M.G., Hua, J., Unschuld, P.G., Lim, I.A.L., Jones, C.K., Margolis, R.L., Ross, C.A., Van Zijl, P.C.M., Li, X., 2016. Quantitative susceptibility mapping suggests altered brain iron in premanifest Huntington disease. Am. J. Neuroradiol. 37, 789–796. https://doi.org/10.3174/ajnr.A4617.
Vonsattel, J.P., Myers, R.H., Stevens, T.J., Ferrante, R.J., Bird, E.D., Richardson, E.P., 1985. Neuropathological classification of huntington's disease. J. Neuropathol. Exp. Neurol. 44, 559–577. https://doi.org/10.1097/00005072-198511000-00003.
Wakana, S., Jiang, H., Zijl, P.C.M. Van, 2003. Fiber Tract Based Atlas of Human Brain 21–29.
Waldvogel, H.J., Kim, E.H., Tippett, L.J., Vonsattel, J.P.G., Faull, R.L.M., 2014. The neuropathology of Huntington's disease. Curr. Top. Behav. Neurosci. 22, 33–80. https://doi.org/10.1007/7854_2014_354.
Ward, R.J., Zucca, F.A., Duyn, J.H., Crichton, R.R., Zecca, L., 2014. The role of iron in brain ageing and neurodegenerative disorders. Lancet Neurol. 13, 1045–1060. https://doi.org/10.1016/S1474-4422(14)70117-6.
Werner, C.J., Dogan, I., Saß, C., Mirzazade, S., Schiefer, J., Shah, N.J., Schulz, J.B., Reetz, K., 2014. Altered resting-state connectivity in Huntington's Disease. Hum. Brain Mapp. 35, 2582–2593. https://doi.org/10.1002/hbm.22351.
Wheeler-Kingshott, C.A.M., Cercignani, M., 2009. About "axial" and "radial" diffusivities. Magn. Reson. Med. 61, 1255–1260. https://doi.org/10.1002/mrm.21965.
Winklewski, P.J., Sabisz, A., Naumczyk, P., Jodzio, K., Szurowska, E., Szarmach, A., 2018. Understanding the physiopathology behind axial and radial diffusivity changes-what do we know? Front. Neurol. 9. https://doi.org/10.3389/fneur.2018.00092.
Wolf, R.C., Sambataro, F., Vasic, N., Depping, M.S., Thomann, P.A., Landwehrmeyer, G. B., Süssmuth, S.D., Orth, M., 2014. Abnormal resting-state connectivity of motor and cognitive networks in early manifest Huntington's disease. Psychol. Med. 44, 3341–3356. https://doi.org/10.1017/S0033291714000579.
Wu, J. rui, Tuo, Q. zhang, Lei, P., 2018. Ferroptosis, a Recent Defined Form of Critical Cell Death in Neurological Disorders. Journal of Molecular Neuroscience 66, 197–206. https://doi.org/10.1007/s12031-018-1155-6.
Yendiki, A., Panneck, P., Srinivasan, P., Stevens, A., Zöllei, L., Augustinack, J., Wang, R., Salat, D., Ehrlich, S., Behrens, T., Jbabdi, S., Gollub, R., Fischl, B., 2011. Automated probabilistic reconstruction of white-matter pathways in health and disease using an atlas of the underlying anatomy. Front. Neuroinf. 5, 1–12. https://doi.org/10.3389/fninf.2011.00023.
Zachariou, V., Bauer, C.E., Seago, E.R., Raslau, F.D., Powell, D.K., Gold, B.T., 2020. Cortical iron disrupts functional connectivity networks supporting working memory performance in older adults. Neuroimage 223, 117309. https://doi.org/10.1016/j.neuroimage.2020.117309.